國立臺灣大學工學院材料科學與工程學系暨研究所

碩士論文

Department of Materials Science and Engineering
College of Engineering
National Taiwan University

Master's Thesis

氧化銅驅動軌道流對自旋軌道矩之增強效應

Enhancement of Spin-Orbit Torque Efficiency via CuO_x -Driven Orbital Currents

黎哲睿

Che-Jui Li

指導教授：白奇峰 博士

Advisor: Chi-Feng Pai, Ph.D.

中華民國 114 年 6 月

June, 2025

doi:10.6342/NTU202502803

國立臺灣大學碩士學位論文
口試委員會審定書
MASTER'S THESIS ACCEPTANCE CERTIFICATE
NATIONAL TAIWAN UNIVERSITY

（論文中文題目）
(Chinese title of Master's Thesis)

CuOx 驅動軌道流對自旋軌道矩效率之增強效應

（論文英文題目）
(English title of Master's Thesis)

Enhancement of Spin-Orbit Torque Efficiency via CuOx-Driven Orbital Currents

本論文係 **黎哲睿** (R11527A23) 在國立臺灣大學材料科學與工程學系國際應用材料工程碩士班完成之碩士學位論文，於民國 114 年 5 月 27 日承下列考試委員審查通過及口試及格，特此證明。

The undersigned, appointed by the Department / International Institute of Applied Materials engineering on 27th/May/2025 have examined a Master's Thesis entitled above presented by **Li, Che-Jui** (R11527A23) candidate and hereby certify that it is worthy of acceptance.

口試委員
Oral examination committee:

白奇峰 白奇峰
（指導教授 Advisor）

黃斯衍 黃斯衍

胡宸瑜 胡宸瑜

系（所、學位學程）主管 Director：蔡豐羽 蔡豐羽

doi:10.6342/NTU202502803

Acknowledgements

很開心能在碩班期間進入白奇峰老師的實驗室，讓我除了增加許多關於自旋電子學的知識，更學到了許多製程、量測和研究上的技術及方法。在就讀碩班期間，我很幸運的能夠接受到許多人的幫助，才能完成這份論文。

首先最感謝白奇峰教授的指導，除了給予我研究方向上的建議也給予了我研究內容許多指導。感謝實驗室諸多學長們的指導和幫助，感謝宸瑜學長在我剛加入實驗室時的指導，教導我幾乎實驗室所有會用到的製程技術和低溫系統量測，也提供我許多量測時的小技巧。感謝佳晉學長教導我 ST-FMR 的操作。感謝唯邦學長、俊逸學長、宇豪學長、子權學長和瑞旭幫忙實驗室的大家維護儀器，除了花了很多時間幫忙我解決儀器上的困擾，也提供我許多寶貴的建議。感謝彥廷學長、兆中學長、詩哲學長、東岳學長和冠豪學長分享許多自己的研究經驗。另外也非常感謝實驗室的胤鈞學長、文翰、珮汝、孟頡、詠絢、冠宇、聖文陪我度過了很有趣的碩士時光。。感謝智晨、書鋒、席維和芃穎陪我出遊探險，還有感謝柏筌、子晏和子騫讓我知道現在學弟有多麼強大。最後感謝我的家人提供我許多支援，讓我能悠哉而無後顧之憂地完成我的碩士學位。

碩士的時光過得很快，中間有過不少失敗也遇到不少障礙，很開心也很遺憾碩士生涯要畫上句號了，很感謝大家陪我走過這段有趣的旅程，我收穫了許多。

doi:10.6342/NTU202502803

doi:10.6342/NTU202502803

摘要

本論文研究透過在鈷鐵硼/鉑的異質結構中加入氧化銅層作為軌道流來源，以提升其自旋軌道矩的效率。研究動機源自近年來對於利用軌道霍爾效應以產生高效率阻尼型(damping-like)轉矩之自旋電子元件的興趣。在本論文中探討了兩種形成氧化銅層的方式：一是具可控氧氣流量的反應性濺鍍，另一是在空氣中自然氧化。透過二次諧波霍爾電壓量測，我們系統性地研究了氧化程度（藉由調整 Q 值與氧化時間）、氧化銅厚度以及鉑厚度對自旋軌道矩效率的影響。

實驗結果顯示使用反應性濺鍍製備的氧化銅可顯著提升阻尼型自旋軌道矩的效率，其最高增幅相較於鈷鐵硼/鉑控制樣品達到 79%。此增強效果對於濺鍍過程中的 Q 值高度敏感，顯示精準控制氧化程度的重要性。自旋軌道矩效率對氧化銅厚度的相關性進一步指出此增強效應主要源於體相（bulk）的效應，而非源自於界面效應。此外，藉由改變鉑厚度也證實，當鉑厚度約為 4 奈米時，其軌道轉自旋（orbital-to-spin conversion）的效率最佳。相比之下，雖然自然氧化產生的氧化銅同樣能產生約為36%的可觀自旋軌道矩增強，但由於其對氧化厚度、氧化程度與界面品質的控制較弱，因此在可調性與重現性方面可能會有較多的限制。

結論而言，本論文的實驗結果證實由氧化銅所產生的軌道霍爾電流能有效提升重金屬／鐵磁材料系統中的自旋軌道矩。實驗結果同時也顯示反應性濺鍍是一種較為可靠且可調的軌道矩工程方法，有機會為未來新一代自旋電子裝置導入軌道矩機制提供了可能的實驗框架。

關鍵字: 自旋電子學、自旋霍爾效應、軌道霍爾效應、自旋軌道矩、二次諧波霍爾電壓量測

doi:10.6342/NTU202502803

doi:10.6342/NTU202502803

ABSTRACT

This thesis investigates the enhancement of spin-orbit torque in CoFeB/Pt heterostructures by adding a CuO_x layer as an orbital current source. The motivation stems from recent studies of utilizing orbital Hall effects to generate efficient damping-like torques in spintronic devices. Two oxidation methods were explored to form the CuO_x layer: reactive sputtering with controlled oxygen flow, and natural oxidation of Cu through ambient air exposure. Using second harmonic Hall voltage measurements, we systematically examined the influence of oxidation level (via Q-factor and oxidation time), CuO_x thickness, and Pt thickness on the resulting SOT efficiency.

The experimental results show that reactively sputtered CuO_x significantly enhances the damping-like SOT efficiency, with the strongest enhancement reaching 79% compared to the CoFeB/Pt control sample. This enhancement is highly sensitive to the Q-factor during sputtering, demonstrating the importance of precisely tuning the oxidation level. The dependence of SOT efficiency on CuO_x thickness further reveals that the enhancement originates from a bulk orbital current effect instead of an interfacial effect. Moreover, varying the Pt thickness confirms that orbital-to-spin conversion is most efficient when the Pt layer is approximately 4 nm thick. In contrast, naturally oxidized Cu also leads to observable torque enhancement, with a maximum increase of about 36%. However, this method offers limited tunability and potentially less consistent performance due to the lack of ability to control oxide thickness, oxidation level, and interface quality.

Overall, these findings confirm that orbital Hall currents generated from CuO_x can effectively enhance SOT in heavy metal/ferromagnet systems. The study demonstrates that reactive sputtering is a reliable and tunable approach to orbital torque engineering

doi:10.6342/NTU202502803

and provides a potential experimental framework for integrating orbital torque mechanisms into next-generation spintronic devices.

Keywords: Spintronics, Spin Hall Effect, Orbital Hall Effect, Spin-Orbit Torque, Second Harmonic Hall Voltage Measurement

doi:10.6342/NTU202502803

CONTENTS

doi:10.6342/NTU202502803

doi:10.6342/NTU202502803

LIST OF FIGURES

doi:10.6342/NTU202502803

doi:10.6342/NTU202502803

doi:10.6342/NTU202502803

doi:10.6342/NTU202502803

doi:10.6342/NTU202502803

doi:10.6342/NTU202502803

LIST OF TABLES

doi:10.6342/NTU202502803

doi:10.6342/NTU202502803

Chapter 1 Introduction

1.1 From Spin to Torque: The Evolution of Spintronics

Modern electronic devices are usually operated by controlling the flow of electric charge. However, as power efficiency and device miniaturization become increasingly concerns, researchers have turned to another intrinsic property of the electron—spin—as a complementary way of storing and manipulating information. This change has given rise to the field of spintronics, which seeks to exploit spin currents to control magnetic states in solid-state systems. By accessing both charge and spin degrees of freedom, spintronics opens the door to faster, more energy-efficient, and nonvolatile information technologies. A crucial requirement in such systems is the ability to generate and deliver spin angular momentum to ferromagnets in a controlled manner, and one of the most successful strategies for accomplishing this is the spin Hall effect.

1.1.1 Spin Hall Effect

The spin Hall effect (SHE) phenomenon was discovered by J.E. Hirsch in 1999 [1]. It provides a way to convert a longitudinal charge current into a transverse spin current in materials with strong spin-orbit coupling. Microscopically, this effect arises from spin-dependent scattering or band structure asymmetries that cause spin-up and spin-down electrons to deflect in opposite transverse directions. The result is the accumulation of spin angular momentum at the sides of the material, forming a spin current that can diffuse into an adjacent ferromagnetic layer. The schematic of how the SHE creates spin

doi:10.6342/NTU202502803

accumulation is illustrated in Figure 1.1. The spin current can be expressed as

$$J_s = \frac{\hbar}{2e}\theta_{SH}(\hat{\sigma} \times J_e) \quad 1.1$$

, where θ_{SH} is the spin Hall angle, $\hat{\sigma}$ is the spin polarization, and J_s are J_e the spin current density and charge current density.

The 5d transition metals such as Pt, Ta, and W are commonly used as spin sources due to their large spin Hall angles and strong spin-orbit interaction [2-5]. These properties make them efficient generators of spin currents. The ability to inject spin angular momentum into ferromagnets without requiring external magnetic fields or magnetic sources has made SHE-based heterostructures central to the development of modern spintronic devices.

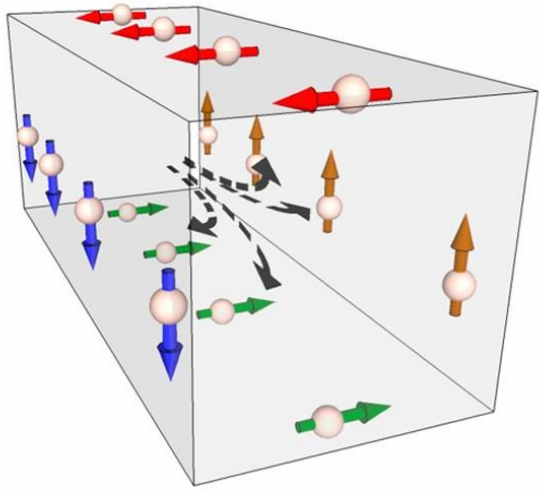

Figure 1.1 Schematic of how the SHE creates spin accumulation with various polarizations on different interfaces. [3]

doi:10.6342/NTU202502803

1.1.2 Spin-Orbit Torque

Once a spin current enters a ferromagnetic layer, it can exert a torque on the magnetization through the transfer of angular momentum—a mechanism referred to as spin-orbit torque (SOT). SOT can originate from the spin Hall effect mentioned in the previous section or the interfacial Rashba effect. Depending on the geometry and symmetry of the system, the spin polarization interacts with the local magnetization to produce two dominant torque components: the damping-like torque, which drives the magnetization toward alignment with the spin direction and enables deterministic switching; and the field-like torque, which acts transversely to the magnetization and can affect its dynamics or assist in switching [6, 7]. The schematic of these two conventional origins of SOT is illustrated in Figure 1.2.

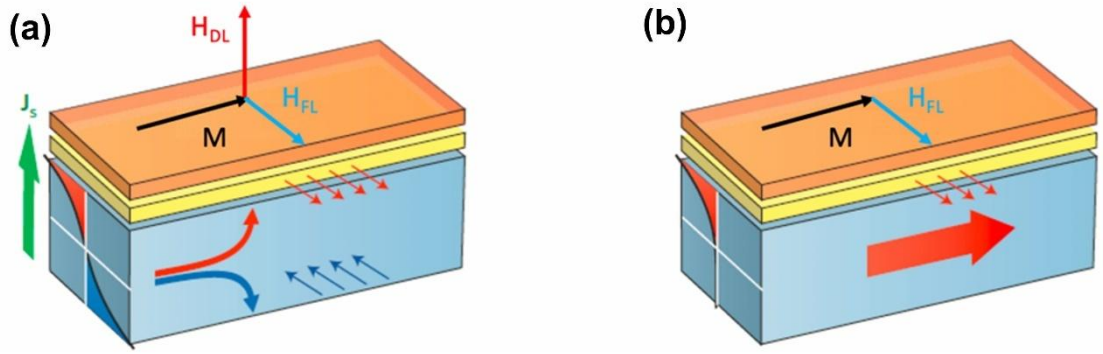

Figure 1.2 Two effects that can originate spin-orbit torques. (a) Spin Hall effect. (b) Interfacial Rashba effect. [8]

The modified LLGS equation is required since the perturbation caused by SOT needs to be taken into consideration [9]. It is expressed as

$$\frac{d\boldsymbol{m}}{dt} = -\gamma \boldsymbol{m} \times \boldsymbol{H_{eff}} + \alpha \boldsymbol{m} \times \frac{d\boldsymbol{m}}{dt} + \gamma \frac{\hbar \theta_{SH} J_e}{2\mu_0 e M_s t_{FM}} \boldsymbol{m} \times (\boldsymbol{m} \times \hat{\sigma}) \qquad 1.2$$

doi:10.6342/NTU202502803

, where θ_{SH} is the spin Hall angle, $\hat{\sigma}$ is the spin polarization, J_e is the charge current density. γ, H_{eff}, and α are the gyromagnetic ratio, effective field, and the Gilbert damping constant respectively.

These torque effects provide a direct and efficient way to manipulate magnetization using purely electrical currents. The ability to achieve deterministic switching without external magnetic fields marks a key advancement in spintronic device design. Spin-orbit torque has thus emerged as a foundational mechanism for next-generation systems, offering compatibility with ultrathin structures and enabling low-power, high-speed operation. Its simplicity and tunability also make it an attractive platform for both applied and fundamental research in spin-based electronics.

1.1.3 Challenges and Limitations

Despite the success of heavy metals in generating spin-orbit torque through the spin-Hall effect, there are still some limitations that restrict further development. One main issue is that the spin Hall angle is an intrinsic property of the material, which is mostly determined by its band structure. As a result, it is not easy to tune or improve the spin current generation efficiency unless a completely different material is introduced. Furthermore, the efficiency of spin current transmission across the heavy metal and ferromagnet interface is strongly affected by the quality of the interface. Factors like roughness, oxidation, or intermixing can reduce the torque efficiency and also make the experimental results harder to interpret clearly.

To overcome these challenges and explore more material options beyond heavy metals, researchers have started to consider orbital angular momentum (OAM) as an alternative way to deliver angular momentum. Unlike spin, orbital momentum may be

doi:10.6342/NTU202502803

easier to generate and control in light transition metals or oxide-based materials. Based on this idea, the field of orbitronics has emerged, which focuses on generating orbital currents and converting them into spin as a new approach to enhance spin-orbit torque. In the next section, the basic concepts of orbitronics will be introduced, along with its possible application in materials like CuO_x.

1.2 Toward Orbitronics: Orbital Angular Momentum in Spin Transport

Recent developments in spintronics have sparked interest in angular momentum transport mechanisms that go beyond the use of spin alone. In particular, orbital angular momentum (OAM)—arising from the electron's motion within atomic orbitals or crystal fields—has gained attention as a complementary degree of freedom that can participate in transport and torque generation. This emerging concept, referred to as orbitronics, explores how orbital currents can be generated, transmitted, and ultimately converted into spin at interfaces. By decoupling angular momentum flow from spin-orbit coupling strength, orbitronics opens the door to new materials and device strategies that were previously inaccessible through conventional spin-based approaches.

1.2.1 Orbital Hall Effect and Orbital Rashba–Edelstein Effect

In conventional spintronics, spin currents are typically generated via the spin Hall effect, which relies on spin-orbit coupling in heavy metals to deflect electrons with opposite spins in transverse directions. However, recent studies have revealed that orbital

doi:10.6342/NTU202502803

angular momentum (OAM) can also participate in charge transport, giving rise to the orbital Hall effect (OHE)—a phenomenon where an electric field drives a transverse flow of OAM without strong SOC [10, 11].

The orbital Hall effect arises from the intrinsic structure of the Bloch wavefunctions and their orbital textures in momentum space. When an in-plane electric field is applied, interorbital hopping between d-orbitals and p-orbitals induces a momentum-dependent orbital polarization. These hybridized states carry finite OAM, and their asymmetric population across the Brillouin zone results in a transverse flow of OAM even in the absence of spin-orbit coupling. This phenomenon constitutes the OHE: electrons moving in opposite directions acquire opposite signs of orbital angular momentum, generating a net orbital current perpendicular to the applied charge current [10, 12]. The OHE is driven by the orbital Berry curvature, and its magnitude depends critically on the symmetry, orbital composition, and hybridization of the bands near the Fermi level. First-principles calculations have demonstrated that the orbital Hall conductivity can be comparable to or even exceed the spin Hall conductivity in various d-orbital transition metals and oxides [11-13].

This mechanism is illustrated schematically in Figure 1.3. Figure 1.3(a) shows the spin Hall effect in a ferromagnetic/nonmagnetic bilayer: an electric field in the nonmagnetic layer generates a transverse spin current, which is injected into the ferromagnet. The injected spin (blue arrow) precession around the local magnetization (black arrows) due to exchange coupling. Figure 1.3 (b) contrasts this with the orbital Hall effect. The electric field drives a transverse flow of orbital angular momentum L_y, visualized as blue and red arrows representing opposite orbital states. Upon entering the ferromagnet, the injected orbital angular momentum is partially converted into a L_z component through a combined action of SOC and exchange interaction. Unlike spin, the

doi:10.6342/NTU202502803

orbital angular momentum does not precession but rather flows through specific momentum space, resulting in a non-precession orbital torque on the magnetization [14].

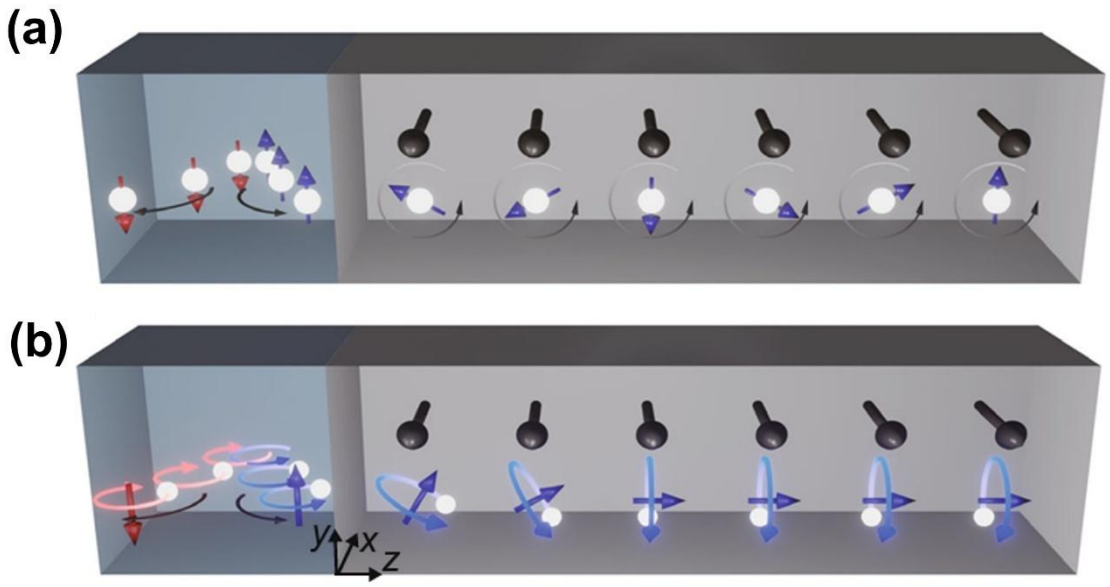

Figure 1.3 (a) Schematic of the spin Hall effect and spin transport in an NM/FM bilayer. (b) Schematic of the orbital Hall effect and orbital transport in an NM/FM bilayer. [14]

At interfaces where inversion symmetry is broken, this orbital transport can also manifest as interfacial orbital accumulation, known as the orbital Rashba–Edelstein effect (ORE). In this mechanism, the electric field induces an imbalance in OAM across momentum space, leading to an interfacial orbital polarization. This polarization is often visualized as a helical orbital texture, where electrons moving in opposite directions carry opposite signs of orbital angular momentum [14-16]. When interfaced with a material possessing strong SOC such as a heavy metal or a ferromagnet, this accumulated OAM can be converted into spin angular momentum, producing an effective field that acts on the magnetization and generates torque. Figure 1.4 illustrates the schematic of how the hybridization of d-orbital and p-orbital in surface oxidized CuO_x constitute the ORE. This

doi:10.6342/NTU202502803

effect is similar to the spin-based interfacial Rashba–Edelstein effect but originates from orbital textures rather than spin textures, and may contribute significantly to field-like torque components, particularly in systems with strong orbital asymmetry at the interface.

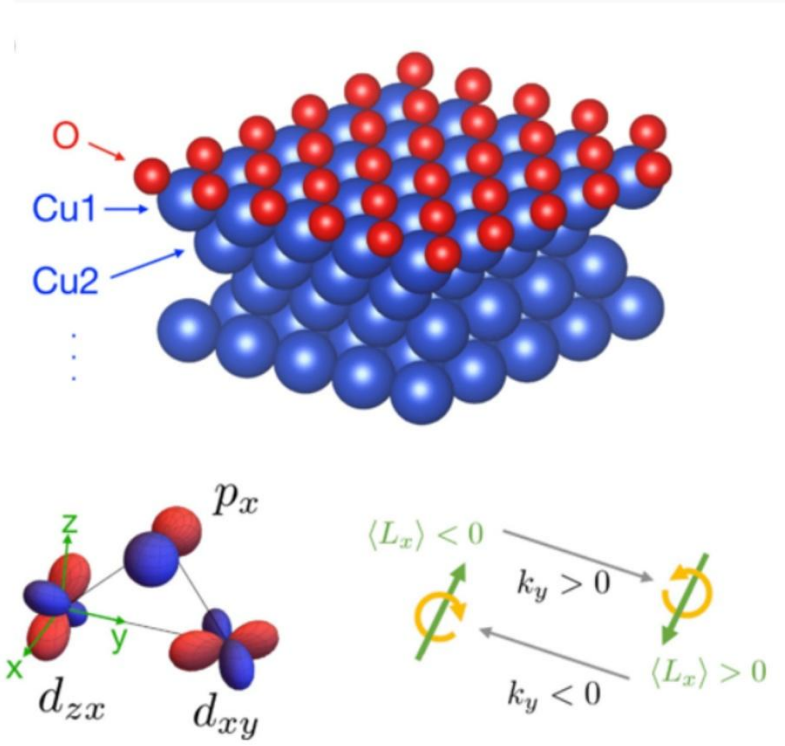

Figure 1.4 Schematic of how the hybridization of d-orbital and p-orbital in surface oxidized CuOx constitute the ORE. [15]

First-principles calculations have shown that the OHE can be significant in a wide range of systems, including transition metals, semiconductors, and two-dimensional materials [15-20]. Importantly, since SOC is not required for OAM transport, the OHE offers a route to angular momentum generation that is decoupled from the limitations of spin-based mechanisms. Both OHE and ORE serve as key mechanisms in orbitronic systems, enabling spin-orbit torque without relying on the intrinsic SOC of the angular momentum source layer.

doi:10.6342/NTU202502803

1.2.2 Orbitally Induced Torque via Orbital-to-Spin Conversion

Although orbital currents can be generated without SOC, they must be converted into spin angular momentum to interact with magnetization and generate torque. This conversion typically occurs at interfaces where SOC is present—either in the adjacent ferromagnet or another insertion layer with strong SOC. The resulting spin accumulation exerts a spin-orbit torque on the ferromagnet, despite the original angular momentum carrier being orbital in nature [10].

Experimental support for orbitally induced torque has been growing. In a Ni/Ta bilayer, A torque sign opposite to that expected from the SHE of Ta but consistent with orbital current predictions is observed, providing direct evidence for orbital torque [10, 21]. Previous studies also demonstrated that orbital Hall currents in Cr could be efficiently converted into spin at Cr/Pt interfaces [22-24]. There is also study indicating that carefully engineered CuN_x layers can exhibit orbital-to-spin conversion, suggesting that light-element nitride systems may serve as effective platforms for orbitally driven spin-orbit torque [25].

As shown in Figure 1.5, two primary pathways for orbitally induced torque have been proposed. R represents the spin-orbit correlation, which determines the relative orientation between spin polarization and orbital polarization. In the first channel, OAM generated in the nonmagnetic layer via the OHE is internally converted into spin via SOC before entering the ferromagnet, which is similar to the traditional SHE to SOT pathway. In the second channel, the orbital current enters the ferromagnet directly and undergoes orbital-to-spin conversion within the ferromagnet itself, producing torque without requiring spin current injection from the nonmagnetic layer [10, 22].

doi:10.6342/NTU202502803

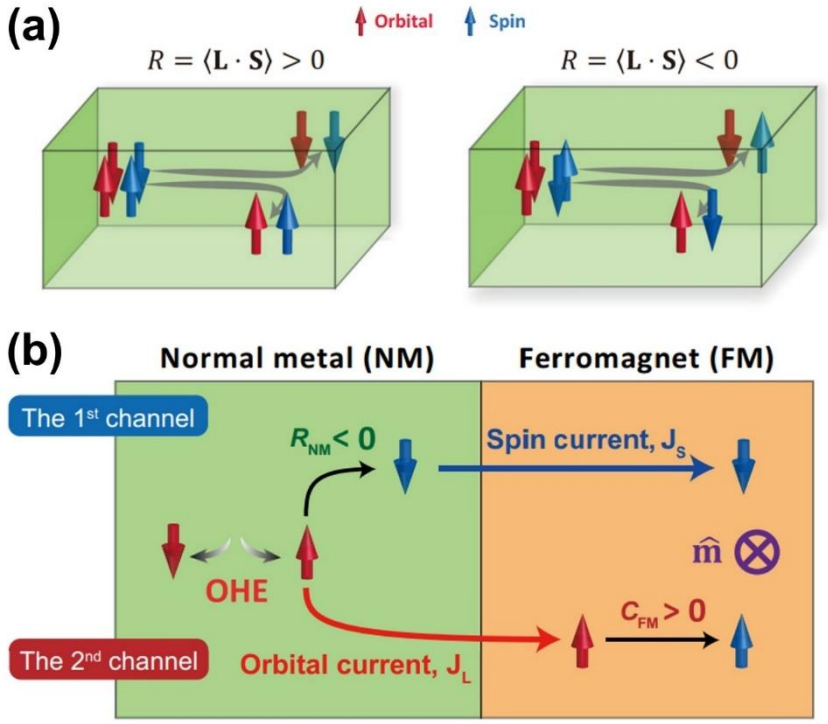

Figure 1.5 (a) The relative orientation between spin polarization and orbital polarization. (b) Schematic of the two pathways for generating the spin current from OHE. [10]

Taken together, these results establish that orbitally generated angular momentum can play a central role in torque generation. Unlike conventional SHE-based approaches, orbital torque mechanisms enable access to a broader range of materials and interfacial tuning strategies, offering a new pathway for spintronic device design.

1.2.3 CuO_x as an Orbital Current Source

Recent advancements in orbitronics have spotlighted CuO_x as a promising candidate for generating orbital currents. Unlike traditional heavy metals that rely on strong spin-orbit coupling to produce spin currents, CuO_x offers an alternative pathway through its unique electronic structure. Its light-element composition and hybridized Cu 3d with O

doi:10.6342/NTU202502803

2p orbitals provide a foundation for OAM transport, particularly when integrated into multilayer spintronic structures.

Several studies have demonstrated that CuO_x can effectively generate orbital currents, which, upon interfacing with ferromagnetic layers, can be converted into spin currents and exert spin-orbit torques. For instance, it is observed that in NiFe/CuO_x -based heterostructures, the orbital Hall effect (OHE) and interfacial orbital Rashba–Edelstein effect (OREE) contribute to efficient torque generation without requiring heavy metals [26, 27]. Also, several previous studies have reported that CoFe/CuO_x or Co/CuO_x bilayers with surface oxidized CuO_x exhibit significant orbital-torque-induced magnetic damping, highlighting CuO_x's efficiency and potential to serve as an active orbital angular momentum source [28-30].

More recent efforts have begun to explore hybrid CuO_x -based structures, where CuO_x is used in combination with heavy metals, such as Pt, to enhance orbital-to-spin conversion. In these systems, CuO_x functions as the orbital current generator, while the adjacent heavy metal layer—rich in SOC—facilitates the efficient conversion of OAM into spin [31, 32]. While this exact configuration with CuO_x remains under continued investigation, analogous studies in Cr/Pt systems by showed that inserting a Pt interlayer substantially increased the SOT efficiency, underscoring the critical role of interfacial SOC in torque transfer [22]. These findings suggest that CuO_x/Pt heterostructures may similarly benefit from strong orbital-to-spin conversion with the insertion heavy metal layer.

A key parameter in these systems is the oxidation state of Cu, which significantly influences the orbital character and thus the orbital current generation. It has been shown that varying the oxidation level of CuO_x can modulate the interfacial orbital Rashba–Edelstein effect and impact torque efficiency in FM/CuO_x structures [33]. This tunability

doi:10.6342/NTU202502803

makes CuO_x particularly attractive, as it allows the electronic structure and OAM generation to be engineered through controlled reactive sputtering or post-growth oxidation processes.

Despite the encouraging results so far, the exact mechanism behind torque generation in CuO_x-based systems is still not fully understood. In particular, it remains unclear how factors like oxidation level**,** interface quality**,** or layer stacking affect how orbital currents are generated and converted into spin. Most previous studies used naturally oxidized Cu or added an extra oxide layer on top to form surface oxidized CuO_x. While this method is useful for enhancing interfacial effects like the orbital Rashba–Edelstein effect, it doesn't provide much insight into bulk orbital Hall transport. To get a clearer picture, a more systematic and controlled study, especially one that carefully tunes the CuO_x oxidation process is needed. This would help better understand how orbital currents behave in these systems and how to use CuO_x more effectively in future spintronic devices.

1.3 Harmonic Hall Voltage Measurement

To explore whether orbital angular momentum contributes to torque generation in spintronic heterostructures, it is essential to use a measurement technique sensitive to the presence of torque and its symmetry and origin. In this study, the harmonic Hall voltage measurement is the primary experimental approach, which offers a powerful way to disentangle the different components of spin-orbit torque.

When a charge current flows through a nonmagnetic/ferromagnetic bilayer, it can generate effective magnetic fields via spin-orbit coupling. As shown in Figure 1.6, these

doi:10.6342/NTU202502803

effective fields cause small shifts in the magnetization direction, which modulate the Hall voltage depending on the angle between the magnetization, current, and applied field. Importantly, the resulting Hall voltage contains both first-harmonic and second-harmonic components, each responding differently to the damping-like and field-like torques. The second harmonic signal, in particular, provides a symmetry-resolved view of the torque and is especially useful in identifying whether the dominant mechanism is bulk spin Hall, interfacial Rashba, or possibly orbitally induced [4, 34-36].

In this thesis, the measurement is carried out using a PHE curve shift measurement, which is a DC harmonic approach [23, 34, 37]. A constant current is applied and the voltage response is recorded as the magnetic field is swept. This method retains the core symmetry sensitivity of harmonic analysis while offering practical benefits in thin-film measurement and signal stability.

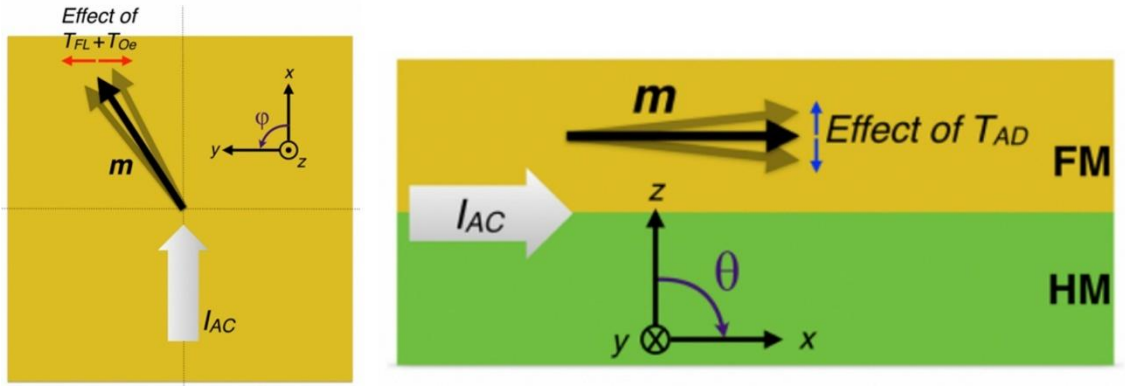

Figure 1.6 Schematic of the harmonic responses from magnetization perturbation. [34]

1.4 Research Motivation

The development of orbitronics has brought new ideas for generating spin-orbit torque through orbital currents. One material that has attracted attention is CuO_x, because

doi:10.6342/NTU202502803

its oxidation level can be changed and it may help create orbital currents that convert into spin at interfaces. However, until now, most research using CuO_x has focused on structures with Co or NiFe as the ferromagnetic layer. There has been little study of using CoFeB, which is a common material in spintronic devices. This is one important motivation for this research. It is still unknown how CuO_x behaves in a CoFeB/Pt-based structure, and whether it can still enhance spin-orbit torque when combined with CoFeB. Studying this system helps us understand how the orbital Hall effect observed in other materials behaves in CoFeB-based system, and whether CuO_x can be used in more practical device structures.

The second and even more important motivation comes from how CuO_x is prepared. In previous studies, CuO_x was formed by natural oxidation—letting a thin Cu layer oxidize in air. However, this process is hard to control and the oxidation level may vary across samples. In this thesis, we use a different method: reactive sputtering, which allows us to grow CuO_x directly during deposition. This gives us better control of oxidation and makes it possible to test whether different oxidation levels lead to different levels of SOT efficiency enhancement. It also allows a more systematic study of how orbital transport changes with chemistry and oxidation level.

The goal of this thesis is to investigate how CuO_x oxidation condition and Pt thickness affect spin-orbit torque in CoFeB/Pt/CuO_x trilayers. We use harmonic Hall voltage measurements to measure damping-like torque. By comparing naturally oxidized and reactively sputtered CuO_x, and by sweeping the Pt and CuO_x thickness, we aim to understand whether the torque enhancement comes from the orbital Hall effect, and how it can be controlled.

doi:10.6342/NTU202502803

Chapter 2 Experiments

2.1 Deposition

2.1.1 Magnetron Sputtering

Magnetron sputtering is a technique widely employed to deposit thin films for various applications, including the fabrication of spintronic devices. In this process, a target material is bombarded by high-energy argon ions (Ar^+) inside a vacuum chamber, resulting in the ejection of target atoms through momentum transfer. These sputtered atoms then travel through the vacuum and condense onto the substrate, forming a thin film [38]. A schematic illustration of a typical DC magnetron sputtering system is shown in Fig. 2.1(a). To maintain an ultra-high vacuum environment and prevent contamination, the deposition chamber is generally equipped with a load-lock system that allows sample transfer without breaking the base pressure.

The efficiency of magnetron sputtering is enhanced by the use of strong permanent magnets placed behind the target. As shown in Fig. 2.1(b) and (c), the magnetic field lines generated by the magnets confine the secondary electrons near the target surface, thereby increasing the ionization probability of the Ar gas. This leads to a denser plasma and a higher sputtering rate compared to conventional diode sputtering. The trajectory of the Ar plasma is guided by the magnetic flux, concentrating the plasma and improving the deposition efficiency. Due to these features, magnetron sputtering allows for relatively high deposition rates while maintaining good film uniformity and low substrate heating, which is particularly advantageous for fabricating multilayer structures required in

doi:10.6342/NTU202502803

spintronic studies.

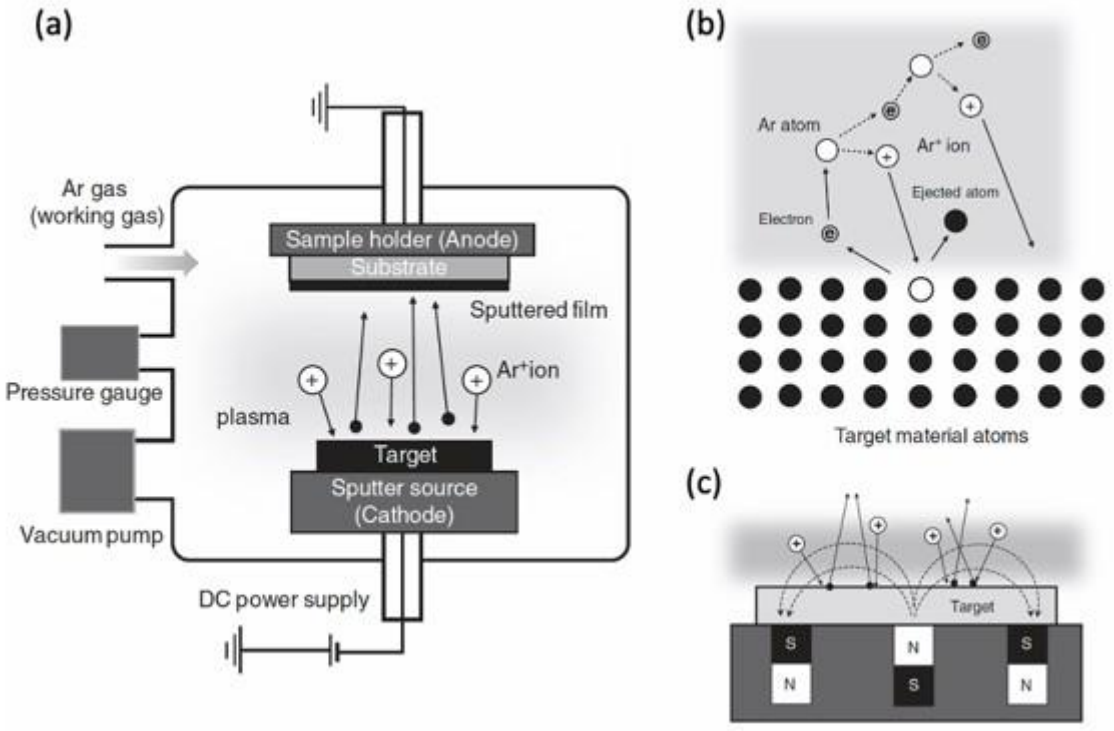

Figure 2.1 (a) Schematic of a DC magnetron sputtering system, where Ar gas is introduced to sustain plasma between the target and substrate. (b) Illustration of the sputtering mechanism: Ar^+ ions strike the target surface and eject atoms through momentum transfer. (c) Magnetic field configuration in the sputter gun. Electrons are confined near the target by magnetic fields, enhancing plasma density and sputtering efficiency. [38]

In this study, all metallic layers, including Pt, CoFeB, Ta, and Cu, were deposited using DC magnetron sputtering. The deposition rates for each target material were carefully calibrated by depositing for a known time and measuring the film thickness using an alpha-step profilometer. The assumption of linear growth rate holds well under standard deposition conditions. The sputter rates calibrated for each material are

doi:10.6342/NTU202502803

summarized in Table 2.1.

Target	Pt	CoFeB	Ta	Cu
Growth rate (nm/s)	0.05263	0.01322	0.02941	0.07692

Table 2.1: Summary of the sputtering rate used in this thesis.

The quality of the thin films produced by magnetron sputtering depends sensitively on several parameters, including the base pressure, working pressure, sputtering power, and target-to-substrate distance. A low base pressure minimizes contamination from residual gases, while an optimized Ar working pressure ensures stable plasma and good film density. In particular, for magnetic heterostructures where spin transport properties are sensitive to interfacial conditions, maintaining clean deposition conditions is crucial. Although the substrate is usually not intentionally heated during deposition, minor substrate heating due to plasma exposure can still influence film properties such as crystallinity and roughness. Therefore, the sputtering parameters were carefully optimized in this work to ensure the reproducibility and high quality of the deposited multilayers.

2.1.2 Reactive Sputtering

Reactive sputtering is a commonly employed method for depositing compound thin films, particularly oxides, nitrides, and carbides, by introducing reactive gases into the sputtering environment. In this process, a reactive gas, such as oxygen (O_2) or nitrogen (N_2), is supplied along with the inert argon gas into the sputtering chamber. During plasma discharge, target atoms are ejected by Ar^+ ion bombardment as in conventional

doi:10.6342/NTU202502803

magnetron sputtering; however, in reactive sputtering, these atoms undergo chemical reactions either in the plasma phase or on the substrate surface to form the desired compound films [39].

Controlling the reactive gas partial pressure is essential to maintain the sputtering system in a stable deposition condition. To quantitatively describe the proportion of reactive gas introduced into the chamber, we define the Q-factor as

$$Q = \frac{\text{reactive gas flow rate}}{\text{reactive gas flow rate} + \text{inert gas flow rate}} \tag{2.1}$$

By adjusting the Q-factor, the reactive sputtering process can be tuned to influence the resulting film properties, including composition, resistivity, uniformity, and crystallinity. For the deposition of uniform and stoichiometric compound films, careful optimization of the Q-factor is necessary. Reactive sputtering offers the advantage of enabling the fabrication of a wide range of compound films, making it a valuable technique in thin-film fabrication for electronic, optical, and magnetic applications.

2.2 Hall bar Fabrication

2.2.1 Photolithography

Photolithography is a key technique in thin-film device fabrication, allowing for precise transfer of designed micro or nanoscale patterns onto a substrate. It relies on the light-induced chemical transformation of a photosensitive polymer known as photoresist. The substrate is first coated with this resist layer, and then exposed to ultraviolet (UV)

doi:10.6342/NTU202502803

light through a photomask that defines the desired geometry [40]. The exposure causes selective changes in the resist's solubility, enabling the pattern to be developed in a solution that removes either the exposed or unexposed regions, depending on whether a positive or negative resist is used. This patterned photoresist can then serve as a temporary mask for subsequent processes such as deposition or etching. The general process of photolithography is shown in Figure 2.2.

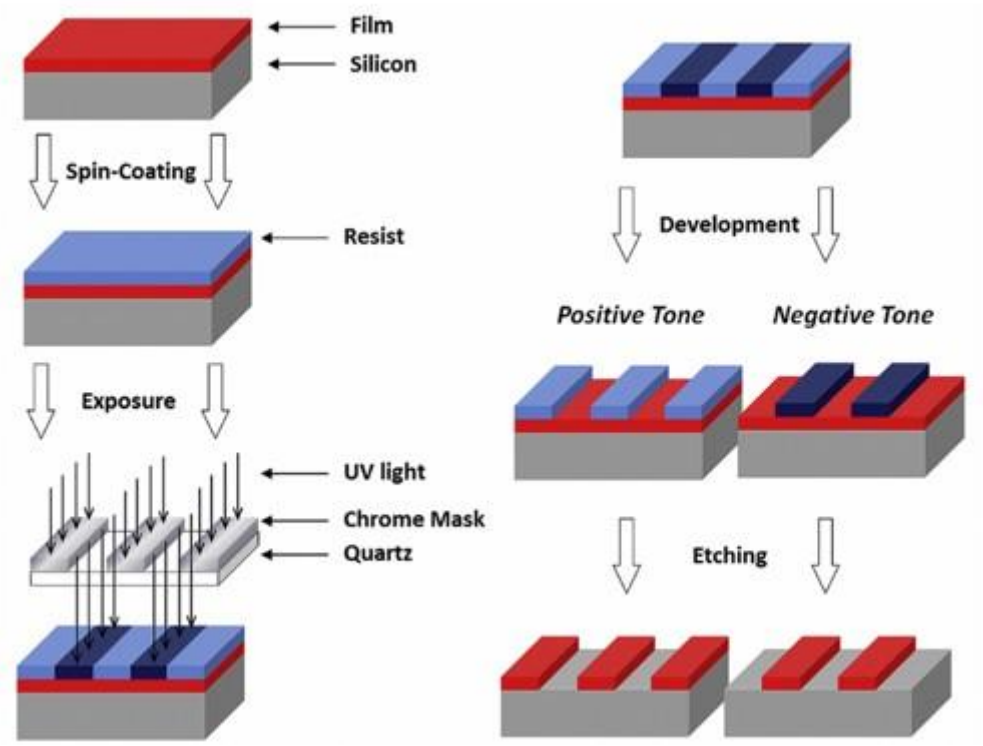

Figure 2.2 The schematic plot for a general photolithography process. [40]

The resolution of the final pattern depends on several factors, including the type of photoresist, exposure wavelength, spin-coating conditions, and development process. Among these, the baking steps are critical in determining resist adhesion and dimensional stability. In lift-off processes, the resist sidewall profile also affects the quality of the final pattern, while for dry etching, the resist thickness and etch resistance must be carefully

doi:10.6342/NTU202502803

optimized. In this study, a negative photoresist was used. The detailed process used in this work is as follows:

1. Substrate cleaning: Samples were immersed in isopropyl alcohol (IPA) and ultrasonicated for at least 30 seconds to remove surface contaminants. They were then baked at 100 ˚C for 60 seconds to eliminate residual moisture.
2. Spin Coating: A negative photoresist (AZ5214E, provided by ECHO CHEMICAL CO. LTD.) was applied using a two-stage spin process: 3000 rpm for 10 seconds followed by 4000 rpm for 30 seconds, yielding a uniform film approximately 1 μm thick.
3. Soft Bake: The coated substrates were soft-baked at 100 ˚C for 100 seconds to evaporate excess solvent.
4. UV Exposure: Samples were exposed to 365 nm UV light for 9.5 seconds using a mercury lamp.
5. Development: The patterns were developed in a 2.38% tetramethylammonium hydroxide (TMAH) solution for roughly 20 seconds. As a negative resist was used, the unexposed areas were removed.
6. Pattern Transfer: The developed resist acted either as an etching mask during IBE or as a lift-off mask. To fabricate devices with electrodes, a second photolithography step was performed after IBE.
7. Lift-off and Cleaning: After metal deposition, acetone was used to remove the resist and any overlying film, finalizing the pattern structure. Then, samples were immersed in IPA again and ultrasonicated for at least 30 seconds to remove the remaining acetone and surface contaminants.

doi:10.6342/NTU202502803

2.2.2 Ion Beam Etching

Ion beam etching (IBE), also known as ion milling, is a physical dry etching process commonly used to define micro and nanoscale patterns in multilayer thin films. Unlike chemically reactive plasma-based techniques, IBE relies purely on physical sputtering by directing a beam of energetic inert gas ions, typically Ar^+ ions, toward the sample surface. These ions, generated in a gridded ion source and accelerated to controlled energies, strike the surface at a specified incidence angle, colliding surface atoms and knocking them out of their regular arrangement area. A schematic representation of the IBE process is shown in Fig. 2.3(a). Because no chemical reaction is involved, IBE is particularly useful for etching chemically stable materials or for applications where surface purity must be preserved.

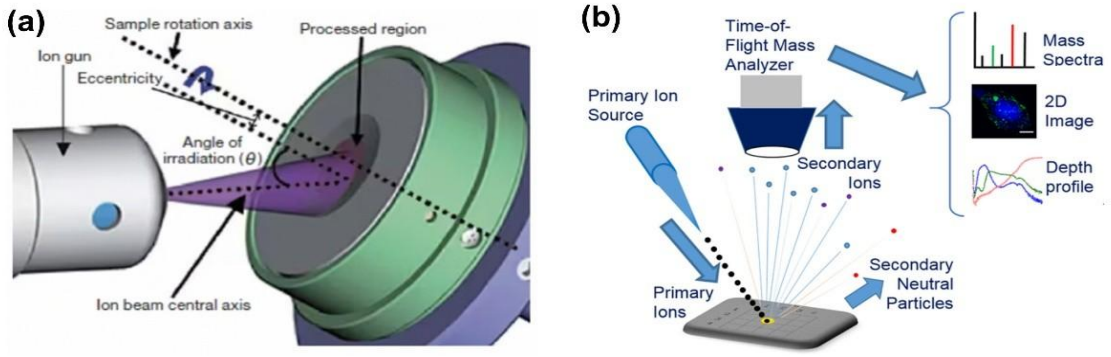

Figure 2.3 (a) Schematic of the ion beam etching process. [41] (b) A schematic diagram illustrating the fundamental principles of ToF-SIMS. [42]

Additionally, secondary ion mass spectrometry (SIMS) is often integrated with an ion beam etching (IBE) system. SIMS enables precise monitoring of the material composition during the etching process. As the ion beam progressively removes surface layers, secondary ions emitted from the sputtered surface are collected and analyzed,

doi:10.6342/NTU202502803

allowing for real-time identification of layer boundaries and compositional changes. This makes SIMS particularly valuable in the fabrication and characterization of multilayer thin-film structures, where accurate control over etch depth is critical. Figure 2.3(b) shows a schematic diagram illustrating the fundamental principles of ToF-SIMS.

In this study, electrode devices were fabricated using a two-step lift-off process followed by IBE. The IBE system enabled an accurate definition of the device geometry by selectively shaping the multilayer thin films into micro-structured patterns, ensuring clean edges and well-controlled lateral dimensions for subsequent transport and magnetic measurements.

2.2.3 Preparation Flow

The samples used in this thesis were fabricated using two different approaches. In both cases, the thin films were deposited onto a clean Si/SiO_2 substrate using magnetron sputtering. As shown in Figure 2.4, the thin film structures investigated in this work can be categorized into three types: 1. CoFeB/Pt2. CoFeB/Pt/CuO_x /Ta 3. CoFeB/Pt/Cu

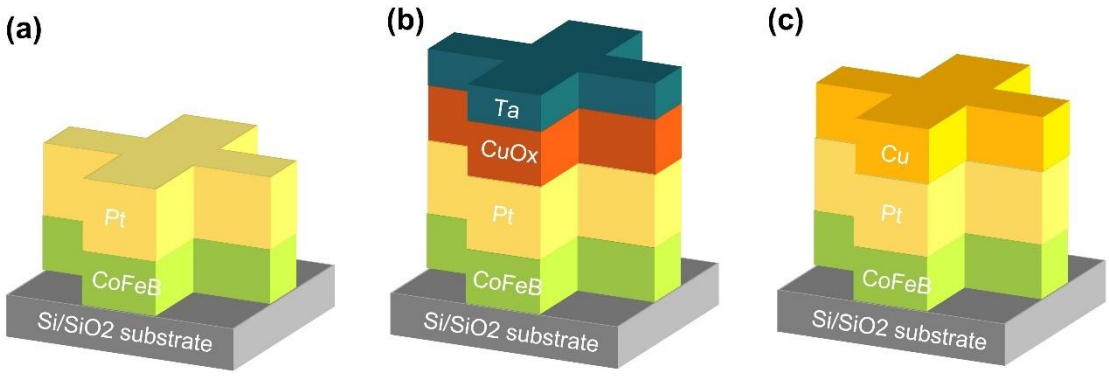

Figure 2.4 Thin film structure used in this thesis. (a) CoFeB/Pt (b) CoFeB/Pt/CuO_x/Ta with reactive sputtering CuO_x (c) CoFeB/Pt/Cu

doi:10.6342/NTU202502803

Depending on the measurement purpose, the sample preparation flow is divided into two types. One type is a simple lift-off device that is used for harmonic Hall voltage measurements. The other type includes patterned electrodes and is used for ST-FMR measurements.

The fabrication process for the lift-off devices is illustrated in Figure 2.5. The desired pattern is first transferred onto the substrate via photolithography. The thin film is then deposited onto the substrate. Finally, remove the unwanted photoresist and any overlying film by acetone, finalizing the pattern structure.

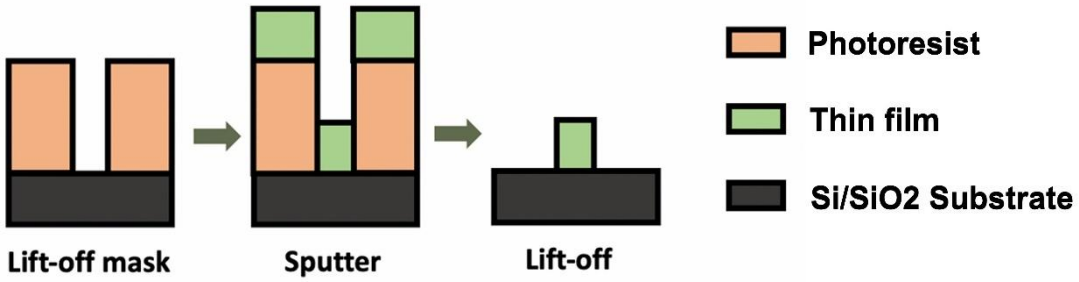

Figure 2.5 The flowchart of fabricated lift-off devices.

The preparation process for fabricating devices with electrodes is shown in Figure 2.6. The full multilayer thin film stack is first deposited on the substrate. Next, photolithography is used to define the desired geometry. The exposed areas are then etched using ion beam etching, and the remaining photoresist is stripped. After that, a second photolithography with different mask is performed. The Ta (80 nm) / Pt (20 nm) electrode is then deposited onto the sample. Finally, remove the unwanted photoresist and any overlying film by acetone and finalize the desired pattern with thin film stack and electrode.

doi:10.6342/NTU202502803

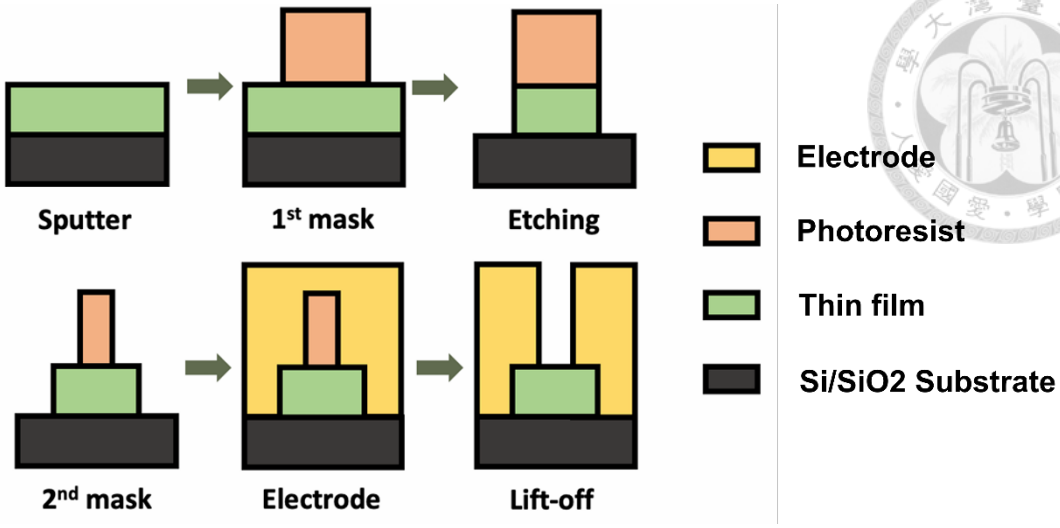

Figure 2.6 The flowchart of fabricated devices with electrodes.

2.3 Measurement

2.3.1 Harmonic Hall Voltage Measurement Setup

To investigate current-induced effective fields in samples with in-plane magnetic anisotropy (IMA), we employed a DC-based PHE curve shift method to extract the second harmonic Hall signal [23, 34, 37]. This technique allows for the extraction of spin-orbit torque components by comparing angular-dependent Hall resistance measured under opposite current directions.

For each angle, the Hall voltage was measured twice: once under +I and once under −I. The symmetric and antisymmetric components of the Hall resistance were then extracted as:

$$R_H^{1\omega} = (R_H^+ + R_H^-)/2$$
$$R_H^{2\omega} = (R_H^+ - R_H^-)/2 \quad (2.2)$$

doi:10.6342/NTU202502803

The $R_H^{1\omega}$ here represents the effect of the conventional planar Hall resistance, which is in the form of

$$R_H^{1\omega} = R_{PHE} \sin 2\varphi \tag{2.3}$$

, while $R_H^{2\omega}$ contains information about the current-induced perturbations and thermal contributions. The damping-like effective field tilts the magnetization into the out-of-plane direction and creates a Hall voltage through the anomalous Hall effect (AHE). The field-like effective field tilts the magnetization into the in-plane direction and generates Hall voltage through the planar Hall effect (PHE). The angular dependence of $R_H^{2\omega}$ was modeled as:

$$\begin{aligned} R_H^{2\omega} &= -(R_{AHE}\frac{H_{DL}}{H_{ext}+H_k^{eff}} + R_{2\omega}^{ANE})\cos\varphi \\ &\quad -(2R_{PHE}\frac{H_{FL}+H_{Oe}}{H_{ext}})\cos\varphi\cos 2\varphi + R_{2\omega}^{PNE}\sin 2\varphi \\ &= R_{2\omega}^{DL+ANE}\cos\varphi + R_{2\omega}^{FL+Oe}\cos\varphi\cos 2\varphi + R_{2\omega}^{PNE}\sin\varphi \end{aligned} \tag{2.4}$$

Here, the first term captures contributions from the damping-like torque and anomalous Nernst effect (ANE), the second from the field-like torque and Oersted field, and the third from the planar Nernst effect (PNE). To extract the spin-orbit torque components, measurements were repeated under different magnetic field strengths. The field dependence of the $R_{2\omega}^{DL+ANE}$ and $R_{2\omega}^{FL+Oe}$ was analyzed using the following relations:

$$\begin{aligned} R_{2\omega}^{DL+ANE} &= -R_{AHE}\cdot H_{DL}\cdot\left(H_{ext}+H_k^{eff}\right)^{-1} + (-R_{2\omega}^{ANE}) \\ R_{2\omega}^{FL+Oe} &= -2R_{PHE}\cdot(H_{FL}+H_{Oe})\cdot(H_{ext})^{-1} \end{aligned} \tag{2.5}$$

From the slope and intercept of the linear fits, the damping-like effective field H_{DL}

doi:10.6342/NTU202502803

, field-like effective field H_{FL}, and the thermal terms (ANE and PNE) were separated. As shown in Figure 2.7, the individual components of the second harmonic Hall signal are distinguished based on their characteristic angular dependencies. By performing measurements under varying magnetic field strengths and analyzing the extracted amplitudes of each angular term, linear fitting can be used to determine the corresponding effective fields.

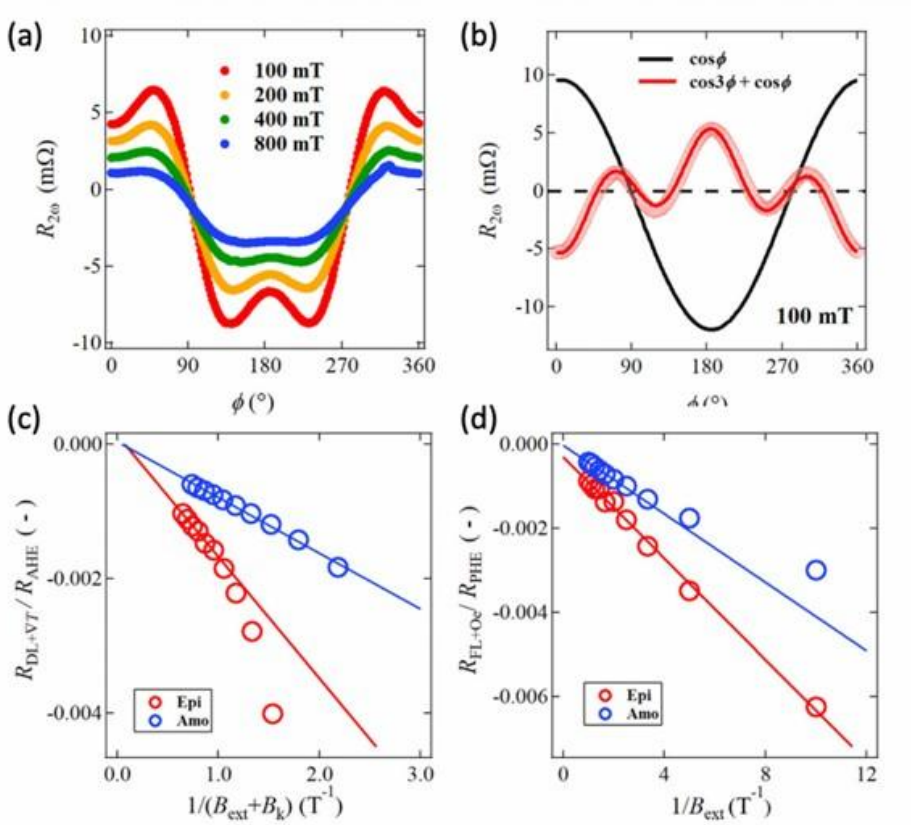

Figure 2.7 Schematic of second harmonic Hall signal under angular dependent measurement. (a) Angular-dependent measurement under different magnetic field strengths. (b) Two main angle dependencies related to SOT-induced perturbation. (c) Field-dependent linear fitting of DL+ANE component. (d) Field-dependent linear fitting of FL+Oersted component. [43]

Before fitting, the values of R_{AHE} and R_{PHE} were calibrated independently. R_{PHE} was extracted by fitting the $R_H^{1\omega}$ which was confirmed to be stable under different field

doi:10.6342/NTU202502803

strengths and current levels. R_{AHE} was estimated through out-of-plane field R_H/H_z sweeps and extrapolation from ST-FMR measurements.

This DC-based method provides improved signal stability and minimizes AC-induced artifacts, making it particularly suitable for measuring torque-induced effects in IMA systems, especially when the signal-to-noise ratio is a concern. The experimental setup is illustrated in Fig. 2.8. A Keithley 2400 source meter was used to apply a constant DC current, while the transverse Hall voltage was recorded using a Keithley 2000 multimeter. The sample was placed under a rotating in-plane magnetic field with fixed amplitude, typically between 1000Oe and 1800Oe, provided by a vector electromagnet. The field angle was swept from 0° to 360°, with the angle defined between the current direction and the magnetic field.

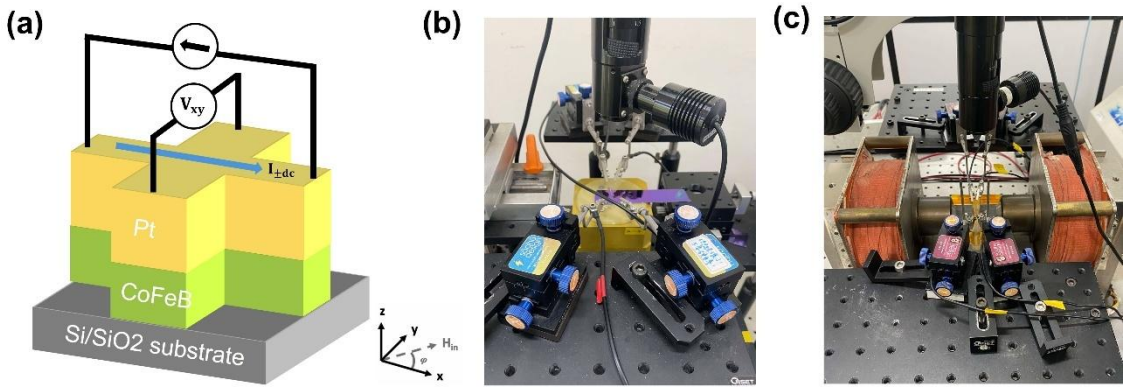

Figure 2.8 (a) Schematic of the harmonic Hall voltage measurement setup. (b) Photo of the GMW probe station. The wafer in the middle is stuck to a micro-stepper to precisely position the specimen, and the yellow object beneath is the projected field vector magnetic. (c) Photo of another probe station with conventional setup. One magnet beneath supplies H_z, which is used for the R_{AHE} slope measurement in this thesis.

doi:10.6342/NTU202502803

2.3.2 Spin-Torque Ferromagnetic Measurement Setup

Spin-torque ferromagnetic resonance (ST-FMR) is a technique widely employed to quantify spin-orbit torques in ferromagnetic heterostructures. In this measurement, a radio-frequency (RF) current is applied to the sample, inducing both an Oersted magnetic field and a spin current via the spin Hall effect in the adjacent heavy metal layer. These excitations drive magnetization precession in the ferromagnetic layer when resonance conditions are met, producing a rectified DC voltage across the device due to the spin rectification effect [9, 44].

The rectified voltage signal, known as the mixing voltage Vmix, is recorded as a function of the applied magnetic field and fitted using a sum of symmetric and antisymmetric Lorentzian functions [9, 45-47]:

$$\begin{aligned} V_{mix} &= \frac{1}{2} I \cdot \Delta R \cdot \sin 2\varphi_0 \cdot (\Re\mathrm{e}[m_x^0] \cdot \cos\delta) \\ &= S \cdot \left(\frac{\Delta^2}{(H - H_0)^2 + \Delta^2} \right) + A \cdot \left(\frac{\Delta (H - H_0)}{(H - H_0)^2 + \Delta^2} \right) \end{aligned} \tag{2.6}$$

Here, H_0 is the resonance field, Δ is the linewidth, and S, A represent the amplitudes of the symmetric and antisymmetric components. The symmetric term arises predominantly from the damping-like torque, while the antisymmetric term includes contributions from the field-like torque and the Oersted field.

Several magnetic and spin-transport parameters can be extracted by performing ST-FMR measurements across multiple microwave frequencies. These include the effective demagnetization field H_{demag}, the Gilbert damping constant α, and the spin-orbit torque efficiency ξ. However, in this thesis, we focus primarily on using ST-FMR measurement to determine the H_{demag}, which reflects the in-plane anisotropy strength of the sample.

doi:10.6342/NTU202502803

The resonance field H_0 obtained at each frequency is fitted using the Kittel formula:

$$f = \frac{\gamma}{2\pi}\sqrt{H_0(H_0 + H_{demag})} \quad (2.7)$$

where f is the applied frequency and γ is the gyromagnetic ratio. This fitting allows for accurate extraction of H_{demag}, which is used to compare magnetic anisotropy across different sample structures. Although the ST-FMR linewidth Δ and line shape components (S and A) also enable the evaluation of α and ξ, these analyses are not pursued in this work.

A standard ST-FMR setup consists of a microwave signal generator (Keysight E8257D in this thesis), a bias tee for signal separation, a ground-signal (GS) microwave probe, and a lock-in amplifier (AMETEK Signal Recovery Model DSP 7265 in this thesis) to detect the DC voltage and a microwave transmission cable that connects the above equipment [48, 49]. A schematic diagram of the full setup of ST-FMR measurement is illustrated in Figure 2.9(a). The microwave signal is modulated at a low frequency (1177Hz in this thesis's measurement) to enable lock-in detection, and the in-plane magnetic field is swept to capture the resonance response.

As shown in Figure 2.9(b), the sample is mounted at the center of an in-plane rotatable electromagnet used to apply the external magnetic field during ST-FMR measurements. A ground-signal (GS) microwave probe is positioned to contact the sample surface. A coplanar waveguide (CPW) electrode, composed of Ta (80 nm) / Pt (20 nm), is integrated with the sample to ensure impedance matching and efficient rf power delivery [50].

doi:10.6342/NTU202502803

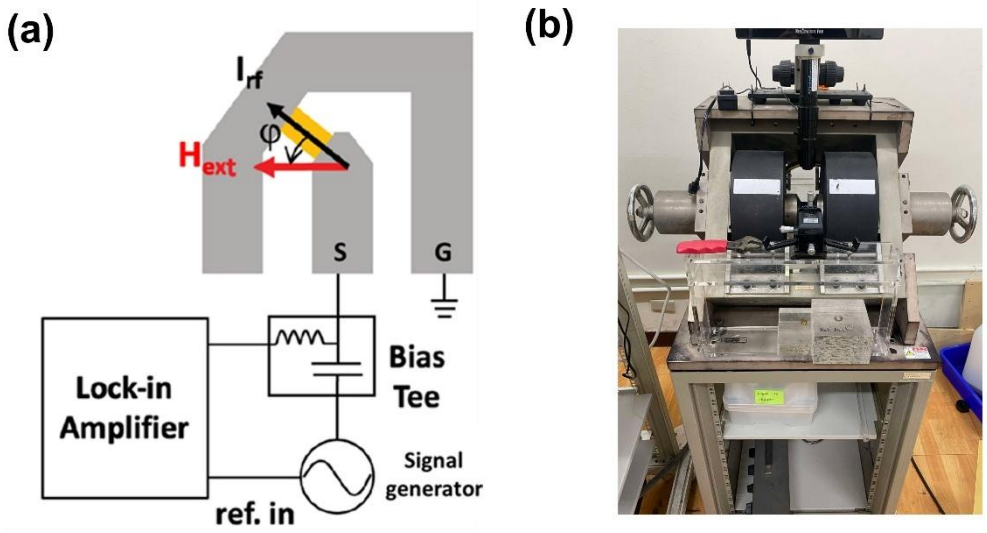

Figure 2.9 (a) Schematic of ST-FMR measurement setup. (b) The sample is placed at the center of an in-plane rotatable electromagnet, with a ground-signal (GS) microwave probe used to deliver the RF signal to the coplanar waveguide (CPW) electrode.

doi:10.6342/NTU202502803

Chapter 3 Results

3.1 Analysis Protocols

Harmonic Hall Voltage measurement is a useful technique to measure the spin-orbit torque efficiency in magnetic heterostructure. In this thesis, I will mainly focus on the magnetic system with in-plane anisotropy.

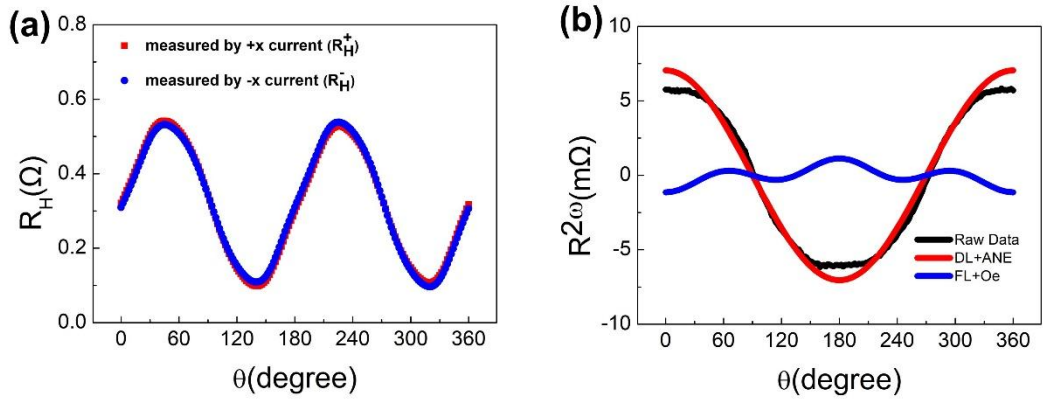

Figure 3.1 PHE curve shift measurement (a) Obtaining PHE curves by measuring Hall voltages under opposite current direction. The first harmonic signal would be the average of these two curves. (b) The second harmonic signal with two main angle dependence terms that are related to SOT-induced effects.

Post-processing is essential to extract the effective spin-orbit torque signals from our measurements, particularly for the planar Hall effect (PHE) curve shift measurement method [23, 34, 37]. Unlike conventional AC harmonic detection, this technique relies on comparing measurements taken under opposite current directions. The first harmonic response is obtained by averaging these measurements, while the second harmonic

doi:10.6342/NTU202502803

component is derived from their difference. They can be expressed by the Equation 2.2.

The first and second harmonic signal of the PHE curve shift measurement is illustrated in Figure. 3.1. Figure. 3.1(a) is the two PHE curves obtained by measuring Hall voltages under opposite current directions. A small difference is observed between the two curves. Figure. 3.1(b) is the second harmonic signal that will be fitted in the following paragraph. With the expression of Equation 2.4, three different angular dependencies are shown and thus we can separate them into three independent components $R_{2\omega}^{DL+ANE}$, $R_{2\omega}^{FL+Oe}$, and $R_{2\omega}^{PNE}$ by their different angular dependents. The second harmonic signal obtained from this procedure contains not only spin-orbit torque contributions but also thermal artifacts. However, the scale of the thermal contribution from the planar Nernst effect (PNE) is less than 0.1% compared to the damping-like torque contributions. Therefore, it is hard to extract from the second harmonic signal and thus can be ignored.

A critical step in harmonic Hall voltage analysis is the field-dependent linear fitting procedure based on Equation 2.5, which enables the separation of spin-orbit torque–induced effective fields from thermoelectric contributions such as the anomalous Nernst effect (ANE). To accurately extract the damping-like and field-like components, the two physical parameters are indispensable: the planar Hall resistance R_{PHE} and the anomalous Hall resistance R_{AHE}.

The R_{PHE} can be obtained directly through in-plane angular measurements of the first harmonic voltage. As for the R_{AHE}, it can be determined by probing its Hall resistance while applying an out-of-plane magnetic field larger than its anisotropy field. However, the measurement setup in our lab is limited to an out-of-plane magnetic field of approximately 2800 Oe, which is insufficient to fully saturate the magnetization for CoFeB-based heterostructures exhibiting strong in-plane anisotropy. As a result, additional steps are required to estimate R_{AHE}.

doi:10.6342/NTU202502803

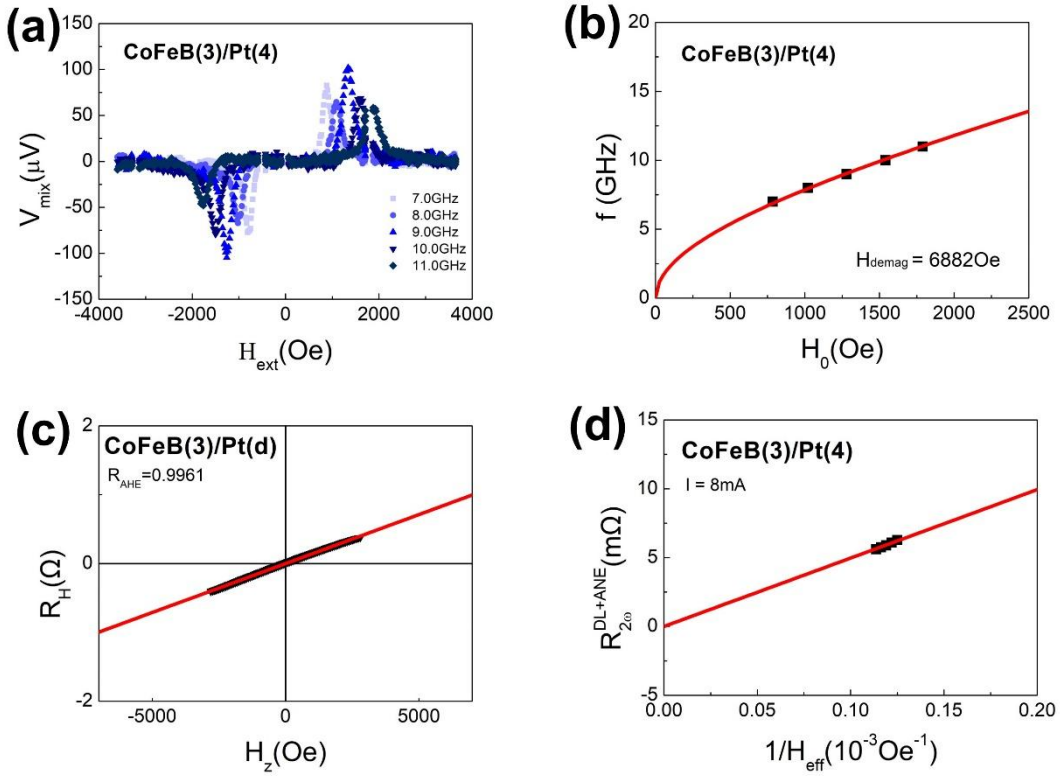

Figure 3.2 Importance parameters for harmonic Hall analysis (a) Raw data of ST-FMR measurement. (b) The Kittel formula fitting of resonance field measured by ST-FMR. (c) The R_{AHE} estimated by combining the slope of Hall voltage under H_z and H_k^{eff} extracted from Kittel formula fitting. (d) Field dependence fitting of damping-like torques and anomalous Nernst effects.

A combination of H_{demag} value extracted by the ST-FMR measurement and R_H/H_z slope can be a good approximation of R_{AHE}. Fig.3.2(a) and (b) show the process of characterization of H_{demag} by ST-FMR measurement. After the H_{demag} value is determined, the expected saturation point $H_k^{eff} \approx H_{demag}$ can be identified with the extrapolation of the R_H/H_z slope shown in Fig.3.2(c). Therefore, the R_{AHE} can be estimated.

Finally, Fig.3.2(d) is the field dependence linear fitting of the extracted term for

doi:10.6342/NTU202502803

damping-like torque and anomalous Nernst effect ($R_{2\omega}^{DL+ANE}$). Based on Eq. 3.3a, the H_{DL} value can be determined from the slope of Fig.3.2(d) and the estimated R_{AHE}. The damping-like SOT efficiency can therefore be calculated from the determined H_{DL} value. This is the basic analysis protocol of this thesis.

3.2 Current Dependence

In the beginning, we need to introduce a current dependence control test to verify the accuracy and consistency of the harmonic Hall measurement protocol. In this section, I use the CoFeB(3)/Pt(4) structure as a reference sample and investigate whether the extracted effective fields scale linearly with the magnitude of the applied current. In this thesis, particular attention is devoted to the damping-like torque because it plays a dominant role in magnetization switching and dynamics in in-plane anisotropy systems. Therefore, we focus on the extraction and verification of damping-like torque throughout the following analyses.

A series of second harmonic Hall measurements were performed under in-plane magnetic fields while sweeping the angle of the field direction. The DC current amplitude was systematically varied, and for each current setting, the second harmonic signal was extracted using the differential method described previously. Representative results are shown in Fig. 3.3(a), where a consistent sinusoidal pattern is observed. The overall amplitude of the second harmonic signal increases with the applied current, while the shape and symmetry of the signal remain similar. This indicates that the response is dominated by spin-orbit torque effects, with negligible influence from thermoelectric artifacts such as the planar Nernst effect (PNE).

doi:10.6342/NTU202502803

To quantify the damping-like torque, the extracted second harmonic voltages were plotted as a function of the inverse of the total effective field. Linear fits were applied based on the previously established model, and the slope of each fit yields the corresponding H_{DL} value. These fitting results are shown in Fig. 3.3(b), where clear linear trends are observed across all current amplitudes, with the intercept that represents the small contribution of thermal offsets.

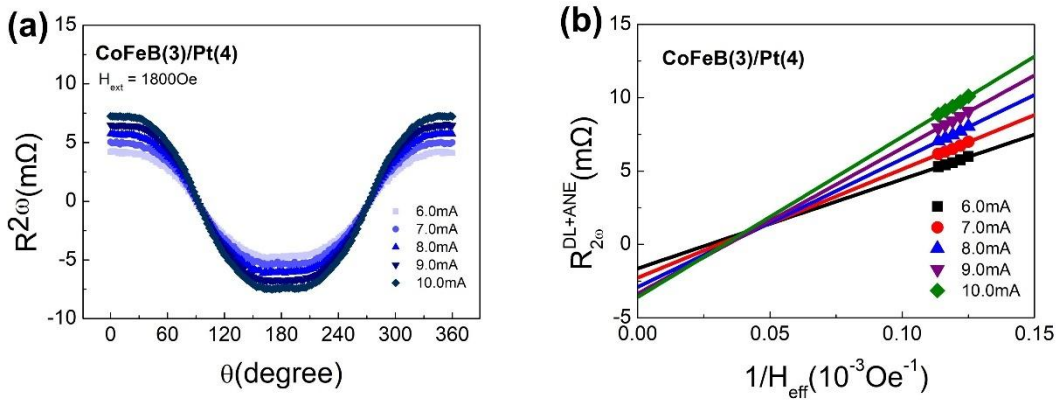

Figure 3.3 Current dependence measurement of CoFeB(3)/Pt(4). (a) Second harmonic signals under different applied currents. (b) Field dependence fitting of damping-like torques and anomalous Nernst effects of CoFeB(3)/Pt(4) under different applied currents.

Finally, the extracted H_{DL} values are plotted against the applied current density, which is calculated by the following equation:

$$J = \left(\frac{t_{HM}/\rho_{HM}}{t_{HM}/\rho_{HM} + t_{FM}/\rho_{FM}}\right) \cdot \frac{I_{applied}}{w \cdot d_{HM}} \tag{3.1}$$

The results are shown in Fig. 3.4(a). A nearly perfect linear relationship is observed, confirming that the damping-like effective field scales proportionally with the applied current density. By simply applying the parameters to the equation illustrated in Equation

doi:10.6342/NTU202502803

3.3, the dimensionless term of damping-like spin-torque efficiencies can therefore be calculated.

$$\xi_{DL} = \frac{2e}{\hbar}\mu_0 M_s t_{FM} w t_{HM} \cdot \left(\frac{\frac{t_{FM}}{\rho_{FM}} + \frac{t_{HM}}{\rho_{HM}}}{\frac{t_{HM}}{\rho_{HM}}} \right) \cdot \left(\frac{H_{DL}}{I_{applied}} \right) \quad (3.2)$$

Fig. 3.4(b) reveals the current-dependent behavior of the damping-like spin-orbit torque efficiency. The variation in ξ_{DL} under different applied currents is less than 2%, which confirms the expected linearity of Hall–driven torque generation and supports the consistency and accuracy of the harmonic Hall measurement protocol used in this work.

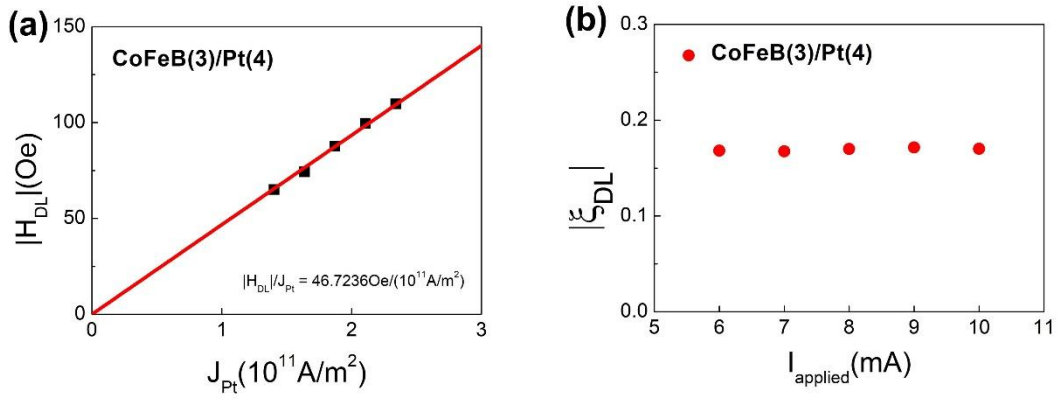

Figure 3.4 (a) The H_{DL}/J plot for CoFeB(3)/Pt(4) measured under different applied currents. (b) The $|\xi_{DL}|$ of CoFeB(3)/Pt(4) measured under different applied currents.

doi:10.6342/NTU202502803

3.3 CoFeB/Pt Control Samples

Traditionally, the characterization of spin-orbit torque requires a bilayer system composed of a heavy metal and a ferromagnetic layer. In this thesis, a CoFeB/Pt bilayer structure is used as the control sample. Following the procedures described in the previous section, harmonic Hall measurements require the determination of several parameters, such as the R_{AHE}. To obtain R_{AHE} , spin-torque ferromagnetic resonance (ST-FMR) measurements must first be conducted. Figure 3.5 shows the Kittel fitting result for the resonance fields obtained through ST-FMR measurement.

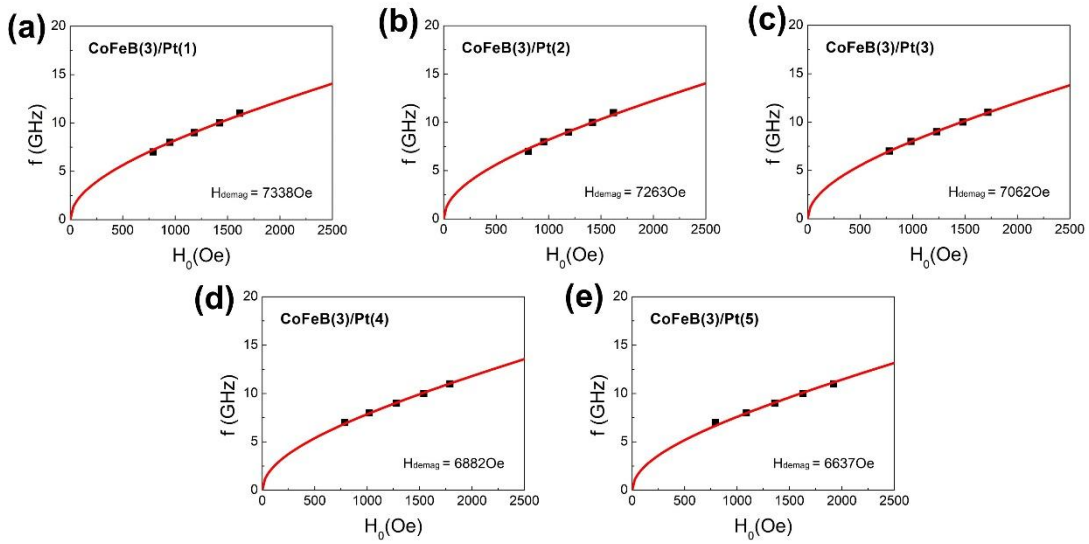

Figure 3.5 The Kittel formula fitting of resonance field measured by ST-FMR.

The expected saturation point, $H_k^{eff} \approx H_{demag}$, can be identified by extrapolating the slope of the R_H vs. H_z curve. Once this point is determined, R_{AHE} can be estimated. Figure 3.6 shows the extracted values of R_{AHE} with different Pt thicknesses. Although R_{AHE} originates from the ferromagnetic layer, its magnitude is influenced by the current shunting effect. As Pt thickness increases, a larger portion of the current flows

doi:10.6342/NTU202502803

through the Pt layer, leading to a decreasing trend in the observed R_{AHE}.

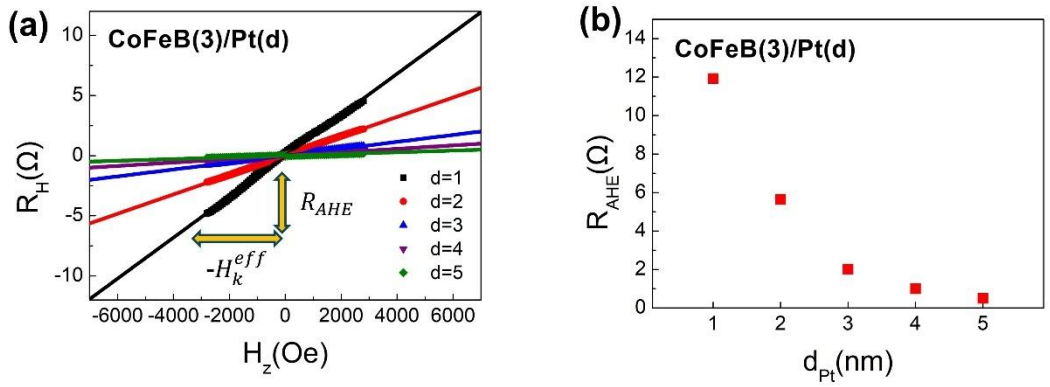

Figure 3.6 Thickness dependence of R_{AHE}. (a) Estimation of R_{AHE} by combining the slope of Hall voltage under H_z and H_k^{eff} extracted from Kittel formula fitting. (b) R_{AHE} vs d_{Pt} relations.

The field-dependent second harmonic signals for different Pt thicknesses are shown in Figure 3.7. Since this work primarily focuses on quantifying the damping-like SOT efficiency, the extracted $R_{2\omega}^{DL+ANE}$ values under varying magnetic fields are fitted using the model described in Eq. 3.2. Applying a larger current improves the signal-to-noise ratio of the second harmonic response, which facilitates more reliable extraction of $R_{2\omega}^{DL+ANE}$. Therefore, higher current is preferred in harmonic Hall voltage measurements.

doi:10.6342/NTU202502803

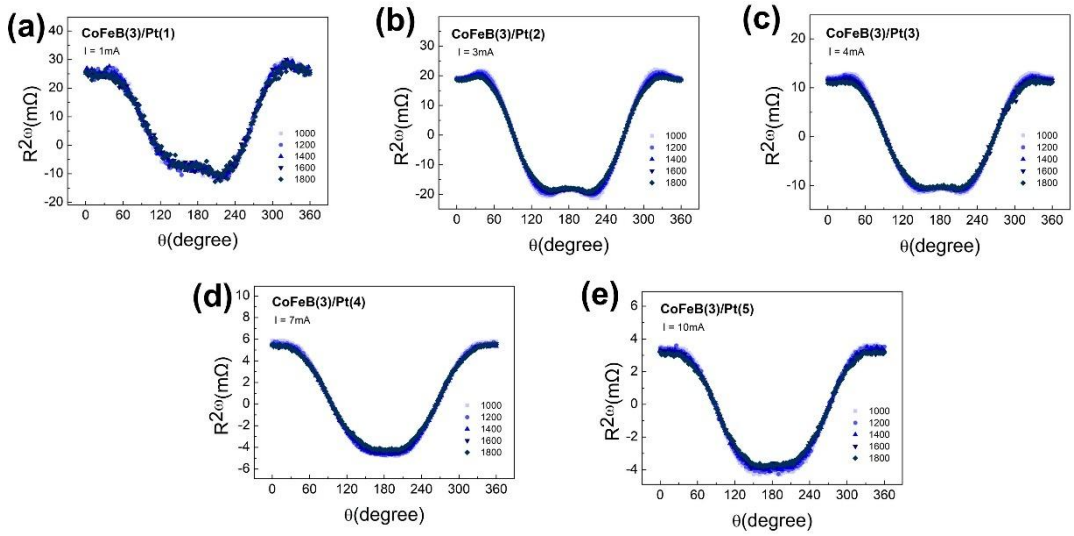

Figure 3.7 CoFeB(3)/Pt's second harmonic raw data.

Figure 3.8(a) shows the linear fitting result of $R_{2\omega}^{DL+ANE}$. The damping-like effective field H_{DL} is obtained by dividing the slope of the fitted line by $-R_{AHE}$, as previously estimated. The current dependence study presented in the earlier section has demonstrated that while the absolute value of H_{DL} changes with the applied current, the ratio of H_{DL}/J remains constant. As a result, the damping-like SOT efficiency can be calculated using Equation 3.2.

The resistivities of CoFeB and Pt are 320 μΩ·cm and 33 μΩ·cm, respectively. Figure 3.8(b) displays the variation of SOT efficiency as a function of Pt thickness. According to the drift-diffusion model [9, 51], the thickness dependence of the heavy metal layer can be described by:

$$|\xi_{DL}(d_{HM})| = |\xi_{DL}^{0}|(1 - \mathrm{sech}\,(\frac{d_{HM}}{\lambda_{sd}}) \tag{3.3}$$

where d_{HM} is the heavy metal thickness, λ_{sd} is the spin diffusion length, and ξ_{DL}^{0} is the bulk damping-like SOT efficiency. The SOT efficiency increases with Pt thickness

doi:10.6342/NTU202502803

and gradually saturates. The spin diffusion length extracted from the CoFeB(3)/Pt(d) control sample series is approximately 1.2536 nm.

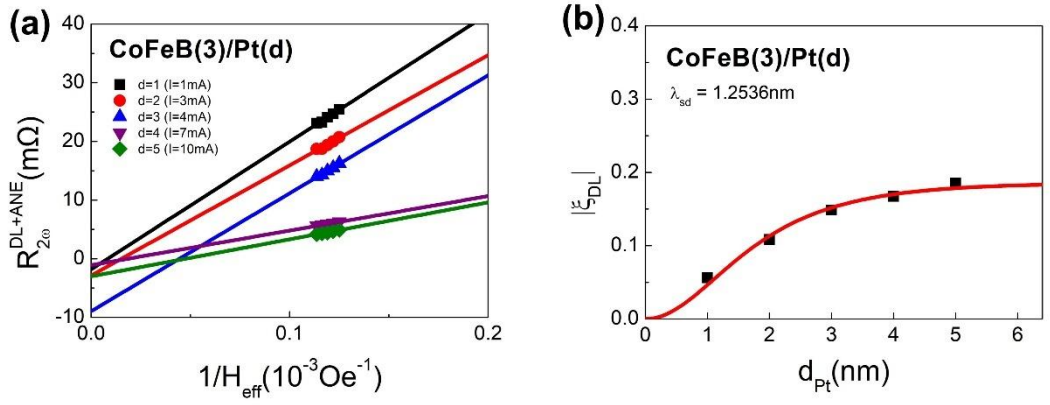

Figure 3.8 (a) Field dependence fitting of damping-like torques and anomalous Nernst effects of CoFeB(3)/Pt with different Pt thickness. (b) Pt thickness dependence Of CoFeB(3)/Pt's DL SOT efficiency with spin diffusion length fitting.

3.4 CoFeB/Pt/CuOx/Ta

In this section, we investigate spin-orbit torque (SOT) enhancement in CoFeB/Pt/CuO_x/Ta heterostructures, where CuO_x acts as an orbital Hall source and Ta serves as a capping layer. The CuO_x layer is deposited via reactive sputtering, allowing precise control over its oxygen content. The objective is to determine whether the orbital Hall effect (OHE) originating from CuO_x can enhance the SOT efficiency of the conventional CoFeB/Pt bilayer. The study is carried out in three stages: first, the reactive sputtering conditions are optimized by identifying the ideal Q-factor; second, the dependence of SOT efficiency on CuO_x thickness is systematically examined; and finally, Pt thickness-dependent measurements are conducted, and the results are compared with

doi:10.6342/NTU202502803

control samples lacking the CuO_x layer.

3.4.1 CuOx Q Dependence

To determine the optimal Q-factor for CuO_x, we first examine its fundamental material properties. As shown in Figure 3.9(a), the sputtering rate remains almost unchanged across different Q-factors. Although there is a slight decreasing trend as the Q-factor increases, the overall variation is very small. Figure 3.9(b) presents the resistivity of CuO_x films grown under varying Q-factors, measured using the standard four-point probe method. The measured CuO_x film is 10nm thick and capping with 2nm Ta. The capping Ta layer is expected to be fully oxidized to insulating TaO_x. Samples with Q = 0%, 1%, 2%, 3%, 4%, 5%, 6%, 9%, 12%, 18%, and 24% were evaluated. As expected, the resistivity increases monotonically with Q. This trend is consistent with the insulating nature of highly oxidized CuO_x.

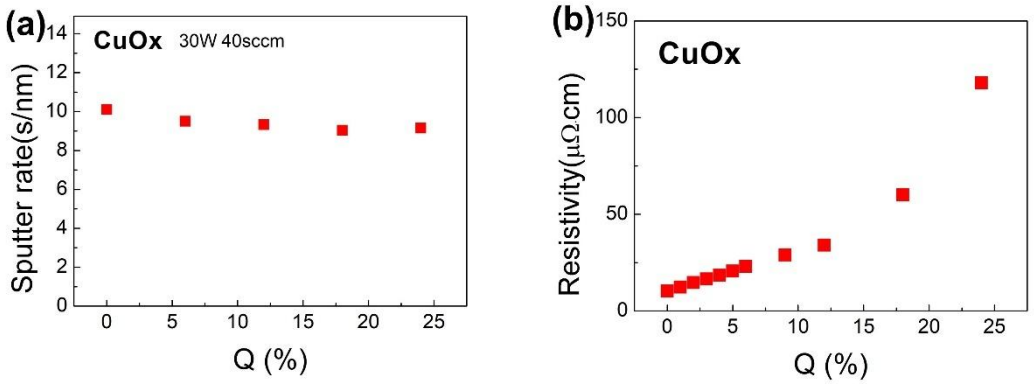

Figure 3.9 Materials properties of CuO_x growth by reactive sputtering, (a) The sputtering rate measured by alpha-step with different Q-factor. (b) The resistivity of CuO_x with different Q-factor.

doi:10.6342/NTU202502803

These electrical measurements are corroborated by Cu 2p X-ray photoelectron spectroscopy (XPS). As shown in Figure 3.10, the Cu 2p spectrum shows narrow peaks without shake-up satellites at Q = 0%. The Cu $2p_{3/2}$ peak is around 932.5 eV, which is consistent with metallic Cu. For Q = 3%, the main peaks broaden slightly, and weak shoulders emerge, indicating the presence of Cu^{+} species associated with Cu_2O. For Q = 6%, the Cu^{2+} satellite peak begins to appear, indicating that CuO has already formed in the sample. At Q = 12%, prominent Cu^{2+} satellite peaks appear around 940-945 eV and 962 eV, confirming the predominant presence of CuO. This evolution confirms a compositional transition from Cu → Cu_2O → CuO with increasing Q.

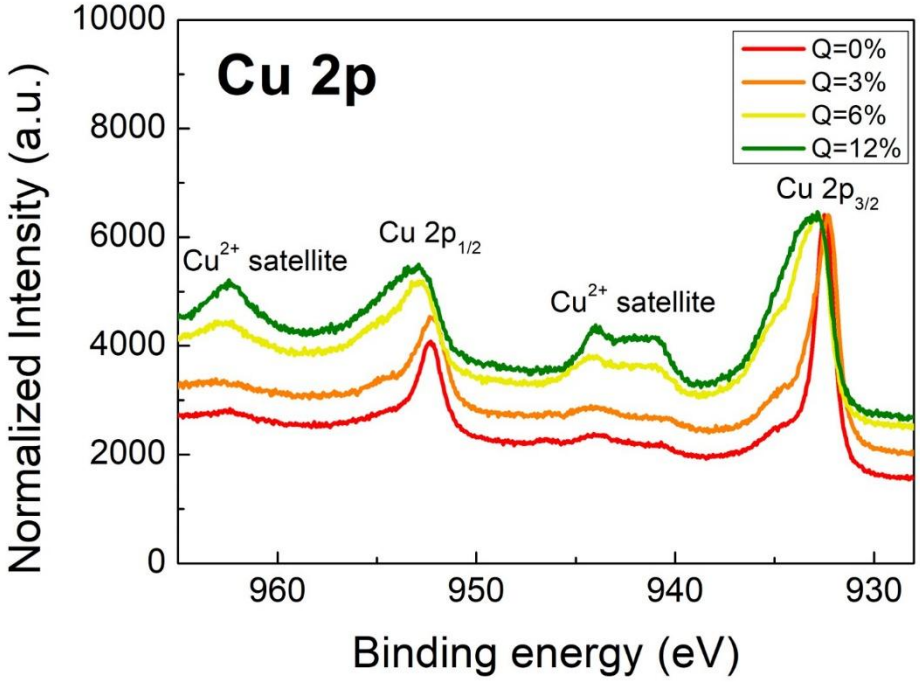

Figure 3.10 The Q dependence of the XPS spectra in CoFeB(3 nm)/Pt(4 nm)/CuOx(3 nm)/Ta(2 nm) samples for the Cu 2p transition. XPS spectral intensities were normalized to the Cu $2p_{3/2}$ peak.

doi:10.6342/NTU202502803

Figure 3.11(a) shows the R_{AHE} of CoFeB(3)/Pt(4)/CuO_x(3)/Ta(2) sample growth under different Q-factor. Although the capping Ta layer is predominantly oxidized into insulating TaO_x, the presence of an additional CuO_x layer leads to a pronounced reduction in R_{AHE} compared to the CoFeB(3)/Pt(4) control sample, which exhibits $R_{AHE} = 0.9961\Omega$.

With the R_{AHE} determined, we apply the analysis protocol described in the previous section to evaluate the SOT efficiency of CoFeB(3)/Pt(4)/CuO_x(3)/Ta(2) heterostructures with different Q-factor. The results are summarized in Figure 3.11(b). As the Q-factor increases, the SOT efficiency initially rises, reaching a peak near Q = 4%, after which it gradually declines. Notably, when Q exceeds 9%, the SOT efficiency falls below that of the sample without any CuO_x layer.

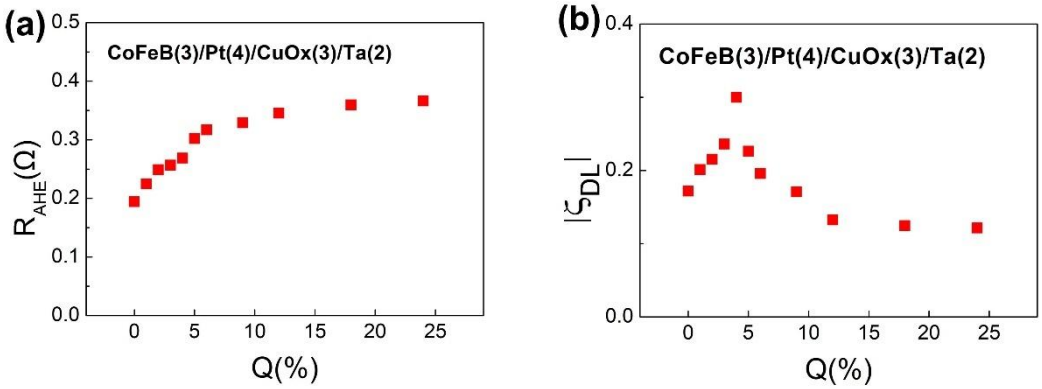

Figure 3.11 (a) R_{AHE} vs Q-factor relations for CoFeB(3)/Pt(4)/CuO_x(3)/Ta(2). (b) Q-factor dependence of CoFeB(3)/Pt(4)/CuO_x(3)/Ta(2)'s DL SOT efficiency.

The sample fabricated with Q = 0%, which represents a non-oxidized Cu layer in the CoFeB(3)/Pt(4)/Cu(3)/Ta(2) structure, exhibits a SOT efficiency of 0.1709. This value is nearly identical to that of the CoFeB(3)/Pt(4) control sample, which has a SOT efficiency of 0.1673. This agreement enhances the reliability of the overall measurement approach,

doi:10.6342/NTU202502803

as it confirms that the additional metallic Cu layer does not affect the SOT efficiency. The observed trend confirms that the oxidation state of CuO_x plays a critical role in modulating the orbital Hall contribution to the overall torque generation.

3.4.2 CuO_x Thickness Dependence

After identifying the optimal oxidation condition through Q-factor tuning, we proceed to investigate the influence of CuO_x thickness on SOT efficiency. In this study, a series of CoFeB(3)/Pt(4)/CuO_x(d)/Ta(2) structures were fabricated with varying CuO_x thicknesses.

The R_{AHE} was measured for each sample using the method described in earlier sections. As shown in Fig. 3.12(a), R_{AHE} decreases monotonically with increasing CuO_x thickness, consistent with increased current shunting through the CuO_x layer.

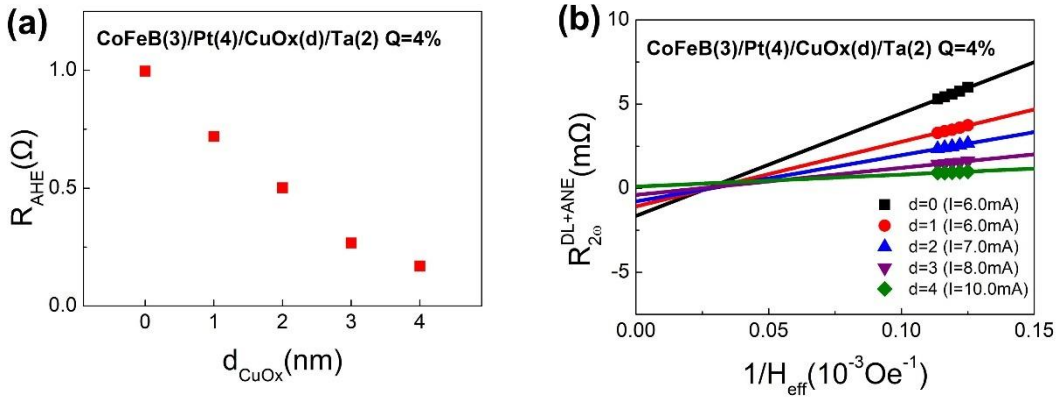

Figure 3.12 (a) R_{AHE} vs d_{CuOx} relations of CoFeB(3)/Pt(4)/CuO_x(d)/Ta(2) samples. (b) Field dependence fitting of damping-like torques and anomalous Nernst effects of CoFeB(3)/Pt(4)/CuO_x(d)/Ta(2) with different CuO_x thickness.

doi:10.6342/NTU202502803

The field-dependent second harmonic measurements for each CuO_x thickness were analyzed to extract the H_{DL}. Linear fittings of $R_{2\omega}^{DL+ANE}$ versus inverse effective magnetic field are presented in Fig. 3.12(b). From these results, the damping-like torque efficiency was calculated and summarized in Fig. 3.13. The result reveals a non-monotonic dependence on CuO_x thickness: the efficiency increases initially with thickness, reaches a maximum at 3 nm, and then declines for thicker CuO_x layers.

This thickness-dependent trend highlights the importance of optimizing the orbital current injection layer. For thinner layers, the orbital angular momentum transfer may be limited, while for thicker layers, the increased CuO_x layer might suppress orbital current transmission. This result also suggests that the observed SOT efficiency enhancement originates from a bulk mechanism, as the efficiency varies with CuO_x thickness. If the effect were purely interfacial, the SOT efficiency would remain largely independent of the CuO_x layer thickness. Among the samples studied, CuO_x with a thickness of 3 nm provides the most efficient torque generation under the given growth and structural conditions.

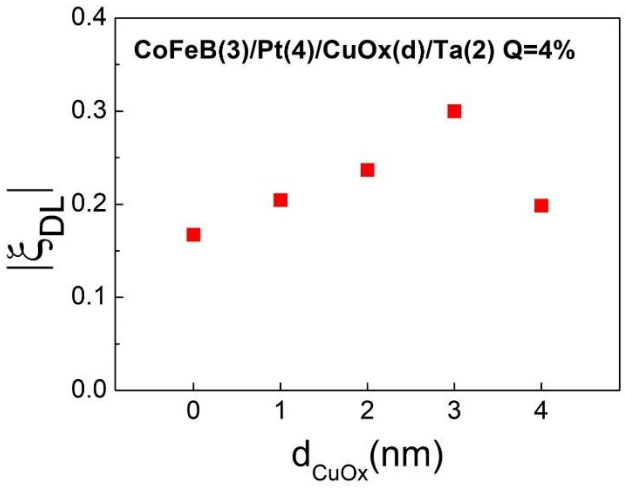

Figure 3.13 CuO_x thickness dependence Of CoFeB(3)/Pt(4)/CuO_x(d)/Ta(2)'s DL SOT efficiency.

doi:10.6342/NTU202502803

3.4.3 Pt Thickness Dependence

Finally, we investigate the influence of Pt thickness on the spin-orbit torque efficiency in CoFeB/Pt/CuO_x/Ta heterostructures. A series of samples with varying Pt thicknesses was fabricated while keeping the CoFeB, CuO_x, and Ta layers the same to compare with the CoFeB/Pt control samples without the CuO_x layer. The capping Ta layer is fully oxidized to insulating TaO_x, so the absence of it in the control samples is acceptable.

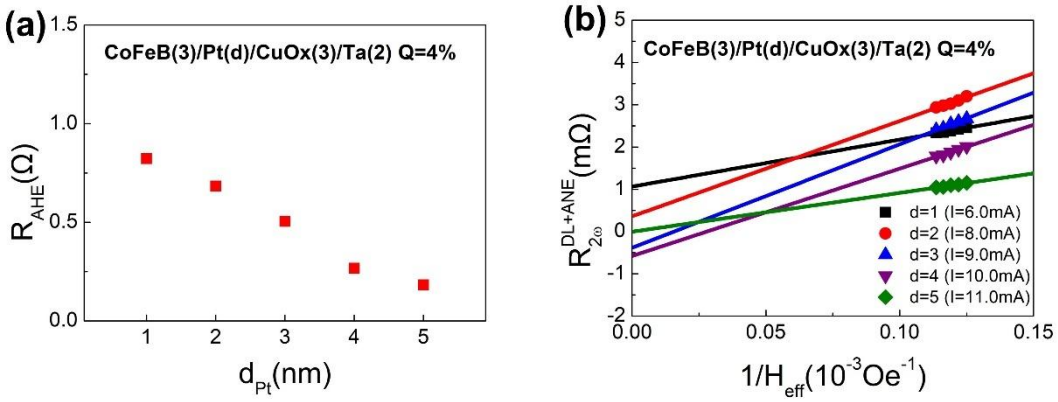

Figure 3.14 (a) R_{AHE} vs d_{Pt} relations of CoFeB(3)/Pt(d)/CuOx(3)/Ta(2) samples. (b) Field dependence fitting of damping-like torques and anomalous Nernst effects of CoFeB(3)/Pt(d)/CuO_x(3)/Ta(2) with different Pt thickness.

Like the method mentioned previously, the R_{AHE} was extracted for each sample. As shown in Figure 3.14(a), R_{AHE} increases monotonically with Pt thickness for both sample series, reflecting enhanced spin accumulation and reduced current shunting effects in the thicker Pt layer.

The H_{DL} was then determined by analyzing the field-dependent second harmonic voltage. Representative linear fittings of $R_{2\omega}^{DL+ANE}$ versus the inverse effective magnetic

doi:10.6342/NTU202502803

field are presented in Figure 3.14(b). From the slopes of these fits and the previously measured R_{AHE}, the H_{DL} can therefore be determined.

The damping-like effective field per unit current density H_{DL} was calculated for both CoFeB(3)/Pt(4) and CoFeB(3)/Pt(4)/CuO_x(3)/Ta(2) structures and is summarized in Figure 3.15(a). This parameter provides a normalized comparison of SOT strength independent of absolute current. A clear enhancement is observed in the samples with a CuO_x layer.

Notably, the 3 nm CuO_x layer growth with Q=4% results in nearly a twofold increase in H_{DL}/J compare to the corresponding control sample. This substantial enhancement highlights the efficiency of orbital current injection from the CuO_x layer and its ability to reinforce damping-like torques at the Pt/ferromagnet stack. The data further support the hypothesis that orbital Hall currents, when properly engineered via reactive sputtering, can serve as a viable mechanism to boost SOT performance beyond conventional heavy metals/ferromagnet structures.

The corresponding spin-orbit torque (SOT) efficiencies for different Pt thicknesses are plotted in Figure 3.15(b). As discussed in the previous section, the CoFeB(3)/Pt control samples exhibit the expected thickness dependence: SOT efficiency increases with Pt thickness and saturates near 5 nm. However, the CoFeB(3)/Pt/CuO_x(3)/Ta(2) samples display a more complex behavior compared to the conventional heavy metal/ferromagnet structure. At 1 nm Pt thickness, the SOT efficiency shows little to no enhancement relative to the control sample. As the Pt thickness increases, a significant improvement emerges, reaching a maximum enhancement near 4 nm. Beyond this point, the advantage offered by the CuO_x layer diminishes, and the SOT efficiency approaches that of the control sample at a larger Pt thickness.

This decrease in enhancement for Pt thicknesses exceeding 4 nm is likely related to

doi:10.6342/NTU202502803

the limited spin diffusion length of Pt. If the orbital-to-spin conversion mainly takes place near the CuO_x/Pt interface, then only the spins generated in that upper region of the Pt layer can travel down to the ferromagnetic layer and contribute to the torque. When the Pt becomes too thick, spins generated farther away from the FM tend to relax and lose their polarization before reaching it. This means that the extra Pt thickness does not contribute much to the overall efficiency. As a result, the difference in SOT efficiency between the CuO_x-inserted and control samples becomes less pronounced at larger Pt thicknesses [52].

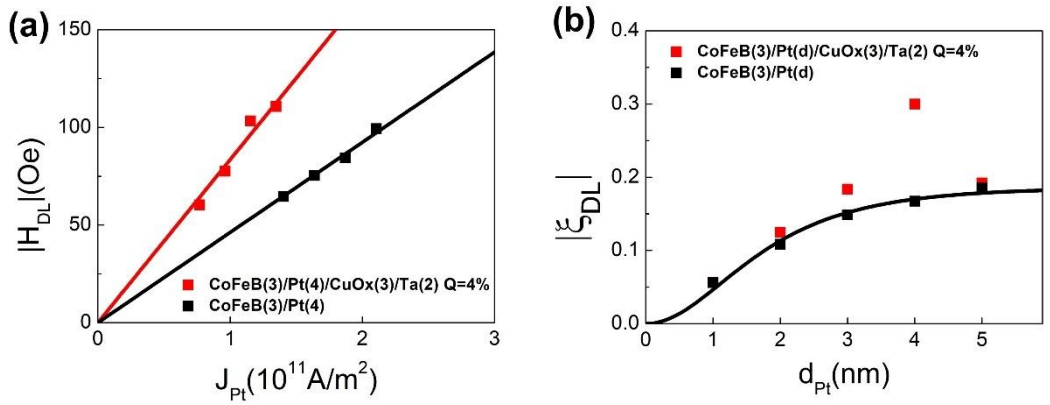

Figure 3.15 (a) Comparison of H_{DL}/J for CoFeB(3)/Pt(4) control sample and CoFeB(3)/Pt(4)/CuO_x(3)/Ta(2) sample. (b) Comparison of Pt thickness dependence Of DL SOT efficiency for CoFeB(3)/Pt(4) control sample and CoFeB(3)/Pt(4)/CuO_x(3)/Ta(2) sample.

These results further reinforce the conclusion that orbital current injection originating from the CuO_x layer can significantly enhance the damping-like spin-orbit torque in conventional heavy metal/ferromagnet systems. The effectiveness of this enhancement is most prominent when the heavy metal layer thickness is appropriately tuned. This study highlights the importance of thickness optimization to maximize the

doi:10.6342/NTU202502803

contribution of orbital torques. Such strategies provide a promising path toward more efficient spintronic devices and energy-efficient magnetization control schemes.

3.5 CoFeB/Pt/Cu with Natural Oxidation

In addition to engineered CuO_x layers deposited by reactive sputtering, several recent studies have explored the use of naturally oxidized Cu as a source of orbital torque. When exposed to ambient conditions, a thin Cu layer undergoes spontaneous surface oxidation, forming a native oxide that may exhibit orbital Hall effects (OHE). Previous works have reported that such naturally formed CuO_x can contribute to damping-like torque generation in heavy metal/ferromagnet heterostructures, likely through interfacial orbital current conversion [31, 33].

However, while natural oxidation offers a simpler fabrication route, it lacks the tunability and consistency provided by reactive sputtering. Parameters such as oxidation depth, stoichiometry, and interface sharpness are difficult to control precisely, leading to potential sample-to-sample variation and unclear oxidation state. Since this thesis primarily focuses on reactive sputtered CuO_x as a systematically controllable orbital torque source, this chapter includes naturally oxidized Cu as a comparative baseline rather than a proposed alternative.

Still, we fabricated CoFeB/Pt/Cu with Cu layer naturally oxidized in air and evaluated the spin-orbit torque efficiency. The results are compared to both CoFeB/Pt/CuO_x/Ta structures and control samples to assess whether native oxidation Cu would produce comparable orbital current contributions.

doi:10.6342/NTU202502803

3.5.1 Oxidation time

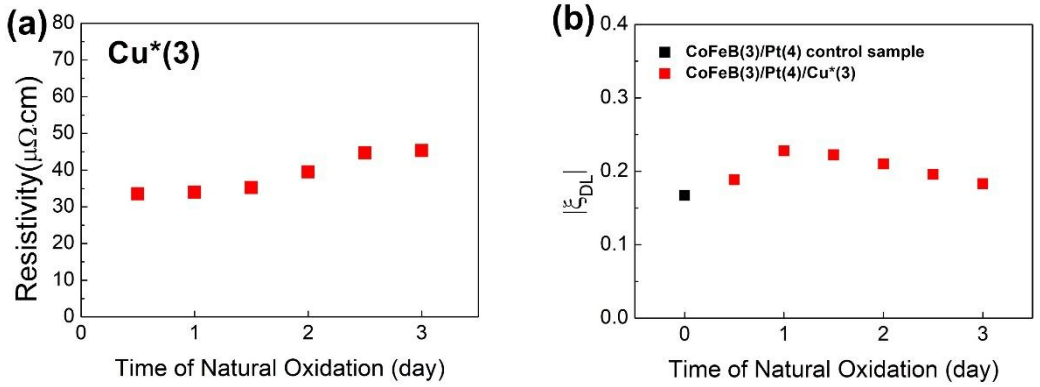

Figure 3.16 (a) The resistivity of top Cu layer as a function of natural oxidation time. (b) The DL SOT efficiency for CoFeB(3)/Pt(4)/Cu(3) sample as a function of natural oxidation time.

To investigate the effect of the natural oxidation Cu layer on spin-orbit torque generation, we performed a time-dependent study on CoFeB(3)/Pt(4)/Cu(3) samples. Figure 3.16(a) shows the resistivity of the 3nm Cu layer as a function of oxidation time, measured every 12 hours after fabrication. The resistivity increases steadily with oxidation time, reflecting the progressive formation of an oxide layer. While the intrinsic resistivity of bulk Cu is approximately 10 μΩ·cm, processing steps during device fabrication lead to a consistently higher baseline in the measured resistivity values.

The corresponding SOT efficiencies are shown in Figure 3.16(b). The efficiency increases with oxidation time, reaching a maximum after 1 day of air exposure, and subsequently decreases. By 3 days, the efficiency drops to a level comparable to that of the CoFeB(3)/Pt(4) control sample. This trend suggests that while initial oxidation can enhance the orbital current generation, extended oxidation may reduce the transparency to orbital angular momentum or introduce scattering effects that limit effective torque

doi:10.6342/NTU202502803

transfer. Similar behavior has been reported in systems where orbital torque generation is mediated by oxidized Cu layers, emphasizing the importance of CuO_x type, oxide thickness, and structural quality in maintaining orbital-to-spin conversion efficiency.

3.5.2 Pt Thickness Dependence

Based on the previous oxidation time study, the CoFeB(3)/Pt(4)/Cu(3) sample naturally oxidized for 1 day exhibited the highest SOT efficiency. To further investigate the influence of Pt thickness under these optimal oxidation conditions, a series of samples with varying Pt thicknesses were fabricated and compared to CoFeB(3)/Pt control samples without the Cu layer.

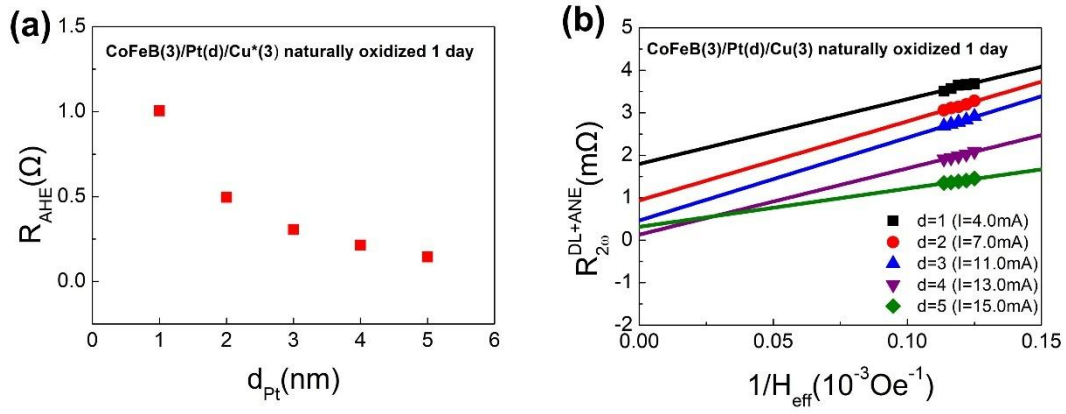

Figure 3.17 (a) R_{AHE} vs d_{Pt} relations of CoFeB(3)/Pt(d)/Cu(3) samples that naturally oxidized 1 day. (b) Field dependence fitting of damping-like torques and anomalous Nernst effects of CoFeB(3)/Pt(d)/Cu(3) samples that naturally oxidized 1 day with different Pt thickness.

The R_{AHE} values extracted for both sample sets are plotted in Figure 3.17(a). As

doi:10.6342/NTU202502803

expected, R_{AHE} decreases with increasing Pt thickness due to enhanced current shunting in the thicker Pt layers. The H_{DL} were extracted through linear fitting of field-dependent second harmonic signals, as shown in Figure 3.17(b) for the naturally oxidized Cu capping samples.

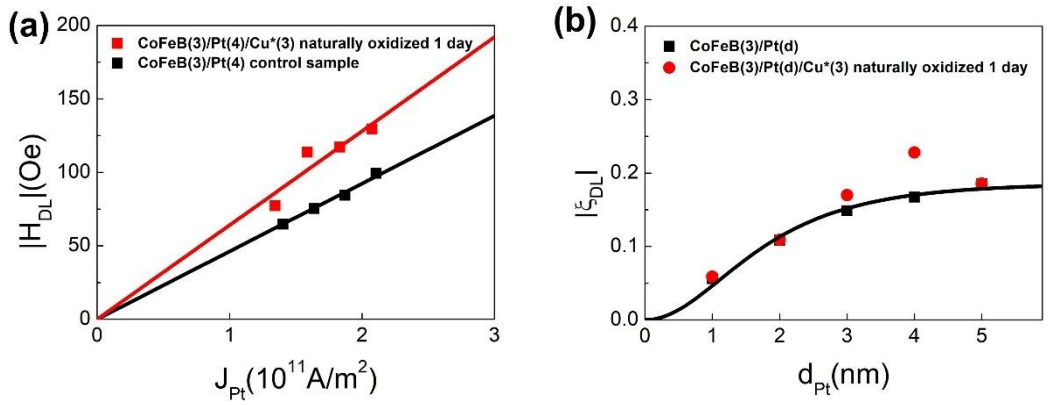

Figure 3.18 (a) Comparison of H_{DL}/J for CoFeB(3)/Pt(4) control sample and CoFeB(3)/Pt(4)/Cu(3) sample that naturally oxidized 1 day. (b) Comparison of Pt thickness dependence Of DL SOT efficiency for CoFeB(3)/Pt(4) control sample and CoFeB(3)/Pt(4)/Cu(3) sample that naturally oxidized 1 day.

The normalized SOT efficacy, represented by the H_{DL}/J ratio, is plotted in Figure 3.18(a) for both the naturally oxidized Cu capping samples and the control samples. The introduction of the Cu(3) layer oxidized for 1 day results in an average enhancement of approximately 36% in H_{DL}/J, confirming that a thin, naturally formed CuO_x layer can contribute additional torque generation.

Figure 3.18(b) compares the spin-orbit torque (SOT) efficiency of different Pt thicknesses between the naturally oxidized and the control samples. The Pt thickness dependence observed in the naturally oxidized samples is similar to the behavior reported

doi:10.6342/NTU202502803

earlier for samples using reactive sputtered CuO_x, but the enhancement is more moderate. When the Pt layer is thinner than 2 nm, little to no improvement is observed, likely due to insufficient orbital-to-spin conversion or poor interfacial transparency. The maximum enhancement occurs at 4 nm Pt, whereas at 5 nm the SOT efficiency of the oxidized sample converges with that of the control sample, indicating a diminished role of the CuO_x layer at larger Pt thicknesses.

This investigation of naturally oxidized Cu layers serves to validate prior studies suggesting that orbital torque can be generated through simple air exposure of metallic Cu. By evaluating the Pt thickness dependence under optimal oxidation conditions (1 day), we confirm that the trend in SOT efficiency closely resembles that observed in reactive sputtered CuO_x systems. Although the overall enhancement is smaller, the consistent behavior supports the interpretation that orbital current generation plays a role in both cases. This section thus provides experimental confirmation of previous reports and establishes a meaningful comparison baseline for the more controllable and tunable CuO_x structures grown via reactive sputtering.

doi:10.6342/NTU202502803

3.6 Discussion

To evaluate and compare the effectiveness of different Cu-derived orbital torque sources, we summarize the key experimental results across three optimized devices: a CoFeB(3)/Pt(4) control sample, a CoFeB(3)/Pt(4)/CuO_x(3)/Ta(2) sample fabricated via reactive sputtering at Q = 4%, and a CoFeB(3)/Pt(4)/Cu(3) sample naturally oxidized for 1 day.

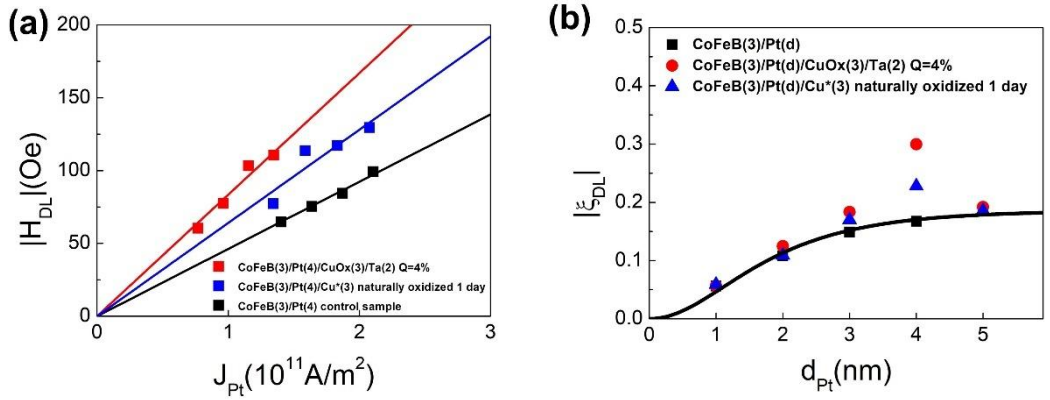

Figure 3.19 Comparison of CoFeB(3)/Pt(4) control sample, CoFeB(3)/Pt(4)/Cu(3) sample naturally oxidized 1 day, and CoFeB(3)/Pt(4)/CuO_x(3)/Ta(2) sample fabricated via reactive sputtering at Q = 4%. (a) H_{DL}/J comparison. (b) Pt thickness dependence Of DL SOT efficiency comparison.

As shown in Figure 3.19(a), the H_{DL}/J reveals a clear ranking in SOT efficacy. The reactive sputtered CuO_x device shows the largest enhancement—approximately 79% higher than the control sample—while the naturally oxidized sample demonstrates a more modest increase of about 36%. This comparison confirms that both reactive and natural oxidation methods can introduce orbital torques but with significantly different magnitudes. The greater enhancement in the reactive sputtered device is likely due to

doi:10.6342/NTU202502803

better control of the quality over the whole CuO_x thickness with a more uniform stoichiometry.

Further insights are provided in Figure 3.19(b), which compares SOT efficiencies of different Pt thicknesses for all three device types. Across all samples, no noticeable improvement is observed for Pt thicknesses below 2 nm or above 5 nm, indicating that for both samples, orbital torque contributions is limited in these regimes. Between 2 nm and 5 nm, however, both CuO_x-based devices exhibit increased efficiency, peaking at 4 nm. The reactive sputtered CuO_x sample not only reaches a higher maximum but also maintains a more pronounced enhancement across the thickness range. In contrast, the naturally oxidized Cu layer shows a similar trend but with a reduced effect.

These comparisons emphasize the critical role of oxidation technique in determining the efficiency of orbital torque generation. While natural oxidation offers process simplicity, its variability and limited tunability lead to smaller and less consistent enhancements. In contrast, reactive sputtering enables more systematic control over CuO_x growth, yielding stronger and more reproducible torque enhancement.

Together, these experimental results provide new insight into the role of CuO_x-driven orbital currents in enhancing spin-orbit torques and establish a direct link between SOT efficiency and CuO_x oxidation control. By systematically comparing reactive sputtered and naturally oxidized CuO_x layers, this thesis demonstrates that while both can act as orbital torque sources, reactive sputtering offers the precision and tunability needed for consistent and scalable enhancement. This work not only confirms the importance of orbital Hall effects in real device structures but also introduces a practical pathway for leveraging them through controllable CuO_x growth, which marks a step forward in the material design of efficient spintronic systems.

doi:10.6342/NTU202502803

Chapter 4 Conclusion

In this thesis, we systematically investigated the generation and enhancement of spin-orbit torque (SOT) in CoFeB/Pt-based heterostructures by introducing CuO_x-driven orbital current sources. Two different approaches for generating orbital torque were compared: (1) reactive sputtering to directly deposit CuO_x layers with controlled oxidation levels, and (2) natural oxidation of Cu in ambient conditions. Through harmonic Hall voltage measurements and systematic variation of Q-factor, CuO_x thickness, Pt thickness, and oxidation time, we demonstrated the strong influence of the oxidation process and structural parameters on the resulting SOT efficiency.

Our results show that inserting a CuO_x layer—particularly when reactively sputtered at an optimal Q-factor—significantly enhances the damping-like SOT efficiency. The best-performing CuO_x-inserted sample exhibited up to 79% enhancement in damping-like spin-orbit torque efficiency compared to the control sample, validating the effectiveness of orbital Hall current generation and orbital-to-spin conversion in these systems. The observed dependence of damping-like spin-orbit torque efficiency on CuO_x thickness further confirms the bulk nature of the orbital torque mechanism. Moreover, by tuning the Pt thickness, we identified that the orbital-to-spin conversion is most effective when the Pt thickness is around 4nm, emphasizing the role of layer engineering in optimizing device performance.

In contrast, naturally oxidized Cu layers offered a more modest 36% enhancement compared to the control sample and also exhibited limited tunability. The similarity in Pt thickness dependence between the naturally oxidized and reactively sputtered CuO_x samples supports the common underlying mechanism of orbital Hall effect-driven torque. This comparison reinforces the conclusion that orbital currents from CuO_x-driven oxides

doi:10.6342/NTU202502803

are capable of enhancing SOT and that the oxidation process plays a central role in determining their magnitude and reliability. While natural oxidation offers process simplicity, its variability and limited tunability lead to smaller and less consistent enhancement. Reactive sputtering enables more systematic control over CuO_x growth, yielding stronger and more reproducible torque enhancement.

In conclusion, this work establishes reactively sputtered CuO_x as a robust, tunable source of orbital torque in metallic heterostructures, offering a scalable pathway for enhancing spin-orbit interactions beyond conventional spin Hall systems. By elucidating the structural and interfacial conditions required for efficient orbital-to-spin conversion, these findings provide both fundamental insight and a practical framework for the engineering of next-generation spintronic devices.

doi:10.6342/NTU202502803

REFERENCE

1. Hirsch, J.E., *Spin Hall Effect.* Physical Review Letters, 1999. **83**(9): p. 1834-1837.

2. Liu, L., et al., *Spin-Torque Switching with the Giant Spin Hall Effect of Tantalum.* Science, 2012. **336**(6081): p. 555-558.

3. Pai, C.-F., *The Spin Hall Effect Induced Spin Transfer Torque In Magnetic Heterostructures.* 2015.

4. Takeuchi, Y., et al., *Spin-orbit torques in high-resistivity-W/CoFeB/MgO.* Applied Physics Letters, 2018. **112**(19).

5. Kontani, H., et al., *Giant Orbital Hall Effect in Transition Metals: Origin of Large Spin and Anomalous Hall Effects.* Physical Review Letters, 2009. **102**(1): p. 016601.

6. Xing, T., et al., *Direct detection of spin-orbit effective fields through magneto-optical Kerr effect.* Physical Review B, 2020. **101**(22): p. 224407.

7. Nguyen, M.-H. and C.-F. Pai, *Spin-orbit torque characterization in a nutshell.* APL Materials, 2021. **9**(3): p. 030902.

8. Gambardella, P. *Introduction to Spin Torques and Spin-Orbit Torques in Metal Layers*. in *Spinmechanics III*. 2015.

9. Liu, L., et al., *Spin-Torque Ferromagnetic Resonance Induced by the Spin Hall Effect.* Physical Review Letters, 2011. **106**(3): p. 036601.

10. Lee, D., et al., *Orbital torque in magnetic bilayers.* Nature Communications, 2021.

doi:10.6342/NTU202502803

12(1): p. 6710.

11. Tanaka, T., et al., *Intrinsic spin Hall effect and orbital Hall effect in 4d and 5d transition metals.* Physical Review B, 2008. **77**(16): p. 165117.

12. Go, D., et al., *Orbitronics: Orbital currents in solids.* Europhysics Letters, 2021. **135**(3): p. 37001.

13. Fukunaga, R., et al., *Orbital torque originating from orbital Hall effect in Zr.* Physical Review Research, 2023. **5**(2): p. 023054.

14. Hayashi, H., et al., *Observation of long-range orbital transport and giant orbital torque.* Communications Physics, 2023. **6**(1): p. 32.

15. Go, D., et al., *Orbital Rashba effect in a surface-oxidized Cu film.* Physical Review B, 2021. **103**(12): p. L121113.

16. Yoda, T., T. Yokoyama, and S. Murakami, *Orbital Edelstein Effect as a Condensed-Matter Analog of Solenoids.* Nano Letters, 2018. **18**(2): p. 916-920.

17. Das, K. and A. Agarwal, *Intrinsic Hall conductivities induced by the orbital magnetic moment.* Physical Review B, 2021. **103**(12): p. 125432.

18. Ghosh, S. and S. Grytsiuk, *Chapter One - Orbitronics with uniform and nonuniform magnetic structures*, in *Solid State Physics*, R.L. Stamps, Editor. 2020, Academic Press. p. 1-38.

19. Li, T., et al., *Giant Orbital-to-Spin Conversion for Efficient Current-Induced Magnetization Switching of Ferrimagnetic Insulator.* Nano Letters, 2023. **23**(15): p. 7174-7179.

doi:10.6342/NTU202502803

20. Go, D., et al., *Orbital pumping by magnetization dynamics in ferromagnets.* Physical Review B, 2025. **111**(14): p. L140409.

21. Hayashi, H., et al., *Observation of orbital pumping.* Nature Electronics, 2024. **7**(8): p. 646-652.

22. Lee, S., et al., *Efficient conversion of orbital Hall current to spin current for spin-orbit torque switching.* Communications Physics, 2021. **4**(1): p. 234.

23. Hu, C.-Y., et al., *Toward 100% Spin-Orbit Torque Efficiency with High Spin–Orbital Hall Conductivity Pt–Cr Alloys.* ACS Applied Electronic Materials, 2022. **4**(3): p. 1099-1108.

24. Liu, Q., et al., *Strong Spin-Orbit Torque Induced by the Intrinsic Spin Hall Effect in Cr1-xPtx.* Physical Review Applied, 2022. **18**(5): p. 054079.

25. Chen, T.-Y., et al., *Tailoring Neuromorphic Switching by CuNx-Mediated Orbital Currents.* Physical Review Applied, 2022. **17**(6): p. 064005.

26. An, T., et al., *Electrical Manipulation of Orbital Current Via Oxygen Migration in Ni(81) Fe(19) /CuO(x) /TaN Heterostructure.* Adv Mater, 2023. **35**(25): p. e2300858.

27. An, T., et al., *Enhanced Spin Current in Ni(81) Fe(19) /Cu-CuO(x) Bilayer with Top and Sideways Oxidization.* Adv Mater, 2023. **35**(14): p. e2207988.

28. Ding, S., et al., *Mitigation of Gilbert Damping in the CoFe/CuOx Orbital Torque System.* Nano Letters, 2024. **24**(33): p. 10251-10257.

29. Kim, J., et al., *Nontrivial torque generation by orbital angular momentum injection in ferromagnetic-metal/Cu/Al2O3 trilayers.* Physical Review B, 2021. **103**(2): p.

doi:10.6342/NTU202502803

L020407.

30. An, H., et al., *Spin–torque generator engineered by natural oxidation of Cu.* Nature Communications, 2016. **7**(1): p. 13069.

31. Ding, S., et al., *Harnessing Orbital-to-Spin Conversion of Interfacial Orbital Currents for Efficient Spin-Orbit Torques.* Physical Review Letters, 2020. **125**(17): p. 177201.

32. Krishnia, S., et al., *Quantifying the large contribution from orbital Rashba–Edelstein effect to the effective damping-like torque on magnetization.* APL Materials, 2024. **12**(5).

33. Zheng, K., et al., *Enhanced torque efficiency in ferromagnetic multilayers by introducing naturally oxidized Cu.* Applied Physics Letters, 2024. **124**(19).

34. Avci, C.O., et al., *Interplay of spin-orbit torque and thermoelectric effects in ferromagnet/normal-metal bilayers.* Physical Review B, 2014. **90**(22): p. 224427.

35. Wen, Y., et al., *Temperature dependence of spin-orbit torques in Cu-Au alloys.* Physical Review B, 2017. **95**(10): p. 104403.

36. Yun, S.J., et al., *Accurate analysis of harmonic Hall voltage measurement for spin-orbit torques.* NPG Asia Materials, 2017. **9**(11): p. e449-e449.

37. Kawaguchi, M., et al., *Current-Induced Effective Fields Detected by Magnetotransport Measurements.* Applied Physics Express, 2013. **6**(11): p. 113002.

38. Tang, D.D. and C.-F. Pai, *MAGNETIC MEMORY TECHNOLOGY: Spin-transfer-torque Mram and Beyond*. 2020: John Wiley & Sons.

doi:10.6342/NTU202502803

39. Musil, J., et al., *Reactive magnetron sputtering of thin films: Present status and trends.* Thin Solid Films, 2005. **475**: p. 208-218.

40. Lawson, R.A. and A.P.G. Robinson, *Chapter 1 - Overview of materials and processes for lithography*, in *Frontiers of Nanoscience*, A. Robinson and R. Lawson, Editors. 2016, Elsevier. p. 1-90.

41. Ito, H. and Y. Inagi, *Hitachi's state-of-the-art ion milling system.* The Hitachi Scientific Instrument News, 2018. **10**: p. 22-29.

42. Jia, F., X. Zhao, and Y. Zhao, *Advancements in ToF-SIMS imaging for life sciences.* Frontiers in Chemistry, 2023. **11**.

43. Gamou, H., et al., *Enhancement of spin current generation in epitaxial α-Ta/CoFeB bilayer.* Physical Review B, 2019. **99**(18): p. 184408.

44. Wang, Y., R. Ramaswamy, and H. Yang, *FMR-related phenomena in spintronic devices.* Journal of Physics D: Applied Physics, 2018. **51**(27): p. 273002.

45. Tulapurkar, A.A., et al., *Spin-torque diode effect in magnetic tunnel junctions.* Nature, 2005. **438**(7066): p. 339-342.

46. Kubota, H., et al., *Quantitative measurement of voltage dependence of spin-transfer torque in MgO-based magnetic tunnel junctions.* Nature Physics, 2008. **4**(1): p. 37-41.

47. Sankey, J.C., et al., *Measurement of the spin-transfer-torque vector in magnetic tunnel junctions.* Nature Physics, 2008. **4**(1): p. 67-71.

48. Petit, S., et al., *Influence of spin-transfer torque on thermally activated*

doi:10.6342/NTU202502803

ferromagnetic resonance excitations in magnetic tunnel junctions. Physical Review B, 2008. **78**(18): p. 184420.

49. Tiwari, D., *Improving signal-to-noise ratio of magnetic tunnel junction based radio frequency detector via spin-torque ferromagnetic resonance.* Review of Scientific Instruments, 2022. **93**(5).

50. *Conventional Coplanar Waveguide*, in *Coplanar Waveguide Circuits, Components, and Systems*. 2001. p. 11-86.

51. Liu, Y.-T., et al., *Determination of Spin-Orbit-Torque Efficiencies in Heterostructures with In-Plane Magnetic Anisotropy.* Physical Review Applied, 2020. **13**(4): p. 044032.

52. Santos, E., et al., *Inverse Orbital Torque via Spin-Orbital Intertwined States.* Physical Review Applied, 2023. **19**(1): p. 014069.

doi:10.6342/NTU202502803